Journal of Wind Engineering & Industrial Aerodynamics 256 (2025) 105963

Contents lists available at ScienceDirect

Journal of Wind Engineering & Industrial Aerodynamics

journal homepage: www.elsevier.com/locate/jweia

Full-scale experimental investigation of wind loading on ballasted photovoltaic arrays mounted on flat roofs

Houssam Al Sayegh [a,*], Arindam Gan Chowdhury [b], Ioannis Zisis [c], Amal Elawady [c], Johnny Estephan [d], Ameyu Tolera [e]

[a] Department of Civil and Environmental Engineering, Florida International University, Miami, FL, 33174, USA
[b] Department of Civil and Environmental Engineering, International Hurricane Research Center, Extreme Events Institute, Florida International University, Miami, FL, 33174, USA
[c] Department of Civil and Environmental Engineering, International Hurricane Research Center, Extreme Events Institute, Florida International University, Miami, FL, 33173, USA
[d] MC Consultants, Inc., 221 W. Hallandale Beach Blvd. Suite 225 Hallandale Beach, FL, USA
[e] Verisk Analytics, 131 Dartmouth Street, Boston, MA, 02116, USA

ARTICLE INFO

Keywords:
Ballasted photovoltaic (PV) systems
Wall of wind
Wind deflectors
Cavity pressure
Correlation
Power spectral density (PSD)
Dynamic amplification factor
Wind induced dynamic effects

ABSTRACT

Ballasted photovoltaic (PV) systems, in comparison to roof-anchored systems, are gaining notable popularity on commercial flat roofs due to the benefits they provide in evading roof penetration and the associated insulation issues. However, the accurate estimation of the aerodynamic uplift forces and their consequent effects on system responses presents a new design challenge. Moreover, possible dynamic effects, characterized by wind induced vibrations, are not accounted for in the design of PV systems in ASCE 7–22, potentially rendering the code design coefficients unconservative. Additionally, the available literature is based on roof anchored PV systems, while experiments in the literature utilizing ballasted PV systems which have distinct behavior and dynamic properties are very limited. The current study aims for a better evaluation of the behavior of ballasted PV systems and the mitigation efficiency of wind deflectors under simulated extreme wind events. To fill this knowledge gap, a 2 x 2 full-scale ballasted PV array model, equipped with wind deflectors and located on a model flat roofed structure was tested at the Wall of Wind (WOW) Experimental Facility (EF). The experimental campaign consisted of aerodynamic and dynamic tests, which permits pressure measurements on the panels under high Reynolds number flow, realistically influenced by the vibrations of the deflectors, as well as capturing of array's dynamic characteristics. The results show that wind deflectors effectively reduce both net area-averaged and point pressure coefficients, particularly under cornering wind directions. While the top surface pressures remained unchanged with the addition of deflectors, the bottom surface pressures experienced a substantial decrease, and the power spectral densities of pressure fluctuations were significantly reduced. Wind deflectors also proved to be efficient in reducing the correlation of instantaneous aerodynamic pressures occurring at different points, reducing the area-averaged peak pressures on the panels and, consequently, reducing net uplift on the entire array. Moreover, the aerodynamic loads were amplified by up to 30% due to dynamic effects caused by the wind induced vibration of the panels. Finally, from the failure assessment tests, a cascading failure mode was observed where the supports are consequently lifted before the entire system is flipped.

1. Introduction

The adverse environmental impact of carbon footprint resulting from the use of fossil fuels for energy production has shifted the general energy sector's orientation towards more sustainable alternatives such as wind and solar energy. As a result, solar arrays are becoming an increasingly common appurtenance on the roofs of residential, commercial, and industrial buildings. In 2022 only, solar power accounted for 50% of all the new electricity-generating capacity in the United States, the largest share in the industry's history (U.S. Solar Market

* Corresponding author.
E-mail addresses: halsa037@fiu.edu (H. Al Sayegh), chowdhur@fiu.edu (A.G. Chowdhury), izisis@fiu.edu (I. Zisis), aelawady@fiu.edu (A. Elawady), johnny.b.estephan@gmail.com (J. Estephan), atolera@verisk.com (A. Tolera).

https://doi.org/10.1016/j.jweia.2024.105963
Received 20 June 2024; Received in revised form 17 November 2024; Accepted 17 November 2024
Available online 22 November 2024

Insight). Ground-mounted systems and low-profile arrays on flat roofs, often found on warehouse-type buildings, constitute a significant sector in the solar photovoltaic (PV) market (Schellenberg et al., 2013). The advancements in PV technology have led to the decrease in PV module costs over the past few years which emphasized the growing significance of reducing expenses related to solar support structures, attachments, and ballast weight. This reduction is now crucial for enhancing the economic feasibility of solar projects (Feldman et al., 2012). Ballasted mounting systems have been experiencing a surge in popularity on the roofs of large warehouses and commercial buildings as they efficiently utilize previously unused real estate and offer a non-intrusive solution that eliminates the need for roof penetration. Additionally, ballasted systems offer the advantage of rapid installation and easy removal, facilitating maintenance and inspection tasks (Kern).

Wind flow over sharp corners of structures leads to the formation of conical vortices and suction bubbles. This results in high suction pressures which translate into strong uplift forces on the roof and its appurtenances, including PV systems (Stathopoulos et al., 2014), (Stathopoulos et al., 2012), (Naeiji et al., 2017). Post hurricane observations show that PV installations endure staggering losses during the strong wind of hurricanes. Extensive failures were documented in rooftop and ground-mounted systems after Hurricane Irma, Maria, and Dorian in 2017 and 2019 (Burgess et al., 2018), (Stone et al., 2020). The challenging aspect of designing solar support structures is the unpredictable nature of the uplift, the deciding criteria for ballast requirements. The uplift is caused by aerodynamic forces, and further amplified by the dynamic response of PV panels subjected to wind-induced vibrations (Moravej et al., 2015), (Naeiji et al., 1868), (Estephan et al., 2022).

Previous studies have addressed the topic of wind loading on solar panels using wind tunnel testing (Stathopoulos et al., 2014), (Naeiji et al., 2017), (Abiola-Ogedengbe et al., 2015), Computational Fluid Dynamics (CFD) analysis (Aly and Clarke, 2023), (Mignone et al., 2021), or a combination of both (Choi et al., 2021). However, most of the wind tunnel experiments utilized small-scale rigid models, while full-scale system-level testing of ballasted PV systems remains mostly unexplored. Conducting large-scale wind tunnel testing of low-rise buildings and their associated appurtenances provides the advantage of a more accurate replication of the structural geometric details and achievement of a closer alignment in Reynolds number (Re) with the real-world prototype than is currently possible with the use of smaller scale models (Naeiji et al., 1868), (Alawode et al., 2023; Tolera et al., 2022; Estephan et al., 2021; Matus, 2018; Azzi et al., 2020a). Thus, large-scale physical tests allow for a more realistic simulation of the wind flows and a better assessment of their effects on structures. This comes with its own limitations such as using limited size appurtenances and underlying structures, and the deficit of low frequency turbulence when compared to the atmospheric boundary layer.

After performing large scale testing on solar panels mounted on residential roofs, Naeiji et al. (2017) concluded that peak force coefficients are dependent on the roof type and tilt angle, with the latter being the most critical parameter. Kopp et al. (2012) performed wind tunnel testing on a 1:30 scale model featuring a 12-row array with 12 modules in each row. The research findings indicated that for low tilt angles, pressure equalization primarily dictates the net wind loading, whereas for higher tilt angles, the loading is governed by array generated turbulence. Moreover, the findings of Kopp et al. (Kopp, 2014) revealed that the wind loads on pressure equalizing arrays with low tilt angles are not affected by the row spacing and chord length. Banks (2013) performed wind tunnel tests on tilted PV panels placed on a flat roofed low-rise building and concluded that the uplift forces are controlled by corner vortices generated by the wind flow.

One aspect of wind tunnel testing of solar panels which was overlooked in past studies is the wind induced vibrations of the panels. The topic was not addressed due to ASCE 7 criteria which indicates that dynamic effects on structures with a natural frequency exceeding 1 Hz can be ignored. However, recent testing on full-scale PV systems proved that systems with higher natural frequencies (~12 Hz) that the 1 Hz criterion may experience significant wind induced vibrations. Moravej et al. (2015) compared the results of full scale and small-scale wind tunnel tests of PV panels; significant discrepancy between the results of the two tests was noticed due to dynamic effects on the full-scale panel. This research effort was expanded by Estephan et al. (2022), where a new experimental-numerical methodology was developed to analytically compensate for wind induced dynamic effects using the dynamic properties of the structure (natural frequency and damping ratio) as inputs.

To reduce wind effects on roofs and rooftop appurtenances, various mitigation strategies such as parapets, vortex suppression devices, and wind deflectors have been previously developed and tested by several researchers. Stathopoulos and Baskaran (1987) and Suaris and Irwin (2010) concluded that the use of parapets is generally beneficial in reducing roof pressures. Surry and Lin (1995) showed that the use geometry modifications such as porous and sawtooth parapets, semi-cylindrical projections, and rooftop radial splitters was efficient in reducing roof corner suctions. Cochran and English (1997) revealed that porous screens across roof corners reduced local and area-averaged uplift loads on the roof. Azzi et al. conducted wind tunnel tests on a large-scale building model and showed that the use of perforated parapets on the roof resulted in a 40% reduction in the peak area-averaged suction pressures (Azzi et al., 2020b). On the other hand, parapets were shown to be not as effective in reducing wind loads on roof-mounted PV arrays (Browne et al., 2013). In this regard, mitigation devices on PV arrays, such as the application of wind deflectors, are currently in use by solar panel racking manufacturers (Enstall, Mibet Energy, Sic Solar, Unirac). Wind deflectors are employed to mitigate the uplift forces on ballasted PV systems (Kudav et al., 2012), thereby reducing the ballast requirement, which can impose additional weight on the roof. Geurts and Van Bentum (Geurts et al., 2014) found that wind deflectors installed on the high sides, or elevated edges, of tilted PV systems resulted in up to 50% reduction in the uplift forces, especially on windward and center panels. Banks (2013) noted that the use of wind deflectors or fairings to protect the high sides of the panels had varied results, but almost always decreased uplift forces on panels under strong vortices originating from a building corner. The aforementioned studies focused on small-scale roof-anchored PV arrays and did not consider ballasted systems, which have distinct dynamic properties due to the lack of a mechanical connection to the roof substrate. Additionally, their failure modes involve sliding and overturning.

This study presents results from wind tunnel testing on a full-scale commercial ballasted PV array mounted on a model flat roof, examining its performance before and after equipping it with wind deflectors. Most, if not all, of the previous well-accepted small-scale PV research have identified limitations in their wind tunnel studies and recommended the execution of field or full-scale laboratory studies to answer questions related to scale, inadequate Reynolds number simulation, and wind-induced dynamic effects. The originality of this full-scale study pertains to two fundamental knowledge advancements as it (1) allows the evaluation of aerodynamic pressures as the wind flow is altered by the vibrations of the wind deflectors (especially, at sufficiently high wind speed(s)), and (2) accurately captures the wind induced dynamic effects on the system under real-world conditions, including the vibrations of the panel glass and wind deflectors, and their effects on the behavior of the system under high wind speeds. Thus, this research represents both the flow conditions on and the structural responses of ballasted PV arrays in the field. These realistic effects are often not simulated in small-scale tests previously reported in the literature. The yielded results bridge the gap between small-scale tests and real-world applications, advancing the understanding of the performance of ballasted PV arrays under real-world extreme winds. The subsequent sections describe the experimental testing procedure, discuss the obtained results, and provide recommendations for enhancing the resiliency of

ballasted PV systems.

2. Methodology

2.1. Model and instrumentation

The study was carried out at the Wall of Wind (WOW) Experimental Facility (EF) at Florida International University (FIU). The Wall of Wind is an open jet, large scale testing facility which utilizes 12 1.8 m (6 ft) diameter fans to generate atmospheric boundary layer (ABL) wind speeds reaching up to 70 m/s (156 mph) (Gan Chowdhury et al., 2017). Despite the WOW's large test section, the full-scale nature of this study limited the examination to just one corner of a typical ballasted PV array on the roof of a large warehouse or commercial building [see Fig. 1].

The primary factor influencing the tilt angle of solar arrays is optimizing electricity generation. Depending on the installation location's latitude, steeper tilt angles may provide improved energy production efficiency. However, they also increase the array generated turbulence (Kopp et al., 2012) and consequently the wind-induced uplift on the array. A survey of products from leading racking manufacturers revealed that most ballasted solar installations are designed with tilt angles that range from 5 to 10°. These common practices are based on maintaining a balance between optimizing electricity generation while limiting the wind uplift on the array. Additionally, the industry standard inter-panel gap ranges from 1.9 cm (0.75") to 2.5 cm (1″) and is essential for effective pressure equalization across the system to reduce the net wind loading. The tilt angle of the used PV array is 10°, the spacing between the panels is 1.9 cm (0.75″), and the spacing between the rows is 0.29 m (0.95 ft). The ballasted PV array was placed on a flat roofed building model that was constructed on site in WOW by a certified contractor with dimensions of 4.9 m W × 5.8 m L × 1.7 m H (16 ft × 19 ft × 5.6 ft). Prior to installing the PV system, a 3.35m × 3.35m (11 ft × 11 ft) area at the center of the roof was covered with Thermoplastic Olefin (TPO) membrane, which is a common type of commercial flat roof covering, to simulate the realistic interaction between the panels and the roof surface. The building model and array dimensions are illustrated in Fig. 2. The ballasted PV system consists of two rows of two PV modules each. The ballasted racking system has four clamps that hold the PV module at the upper and lower edges and rests on four supports per module. Each support consists of a base which rests on two rubber pads to prevent sliding and roof abrasion. Each module within the system is equipped with a wind deflector; the deflectors consist of pliable metal sheets perforated in the middle and fitted to the back of the system [see Fig. 3]. Furthermore, the system features steel rails to add stiffness and interconnect the system; the rails also form a tray to allow for ballasting. Different ballast configurations were tested under different wind speeds: Configuration A refers to using one ballast per panel, B for two ballasts, C for three ballasts, and D for four ballasts. Each ballast consisted of a

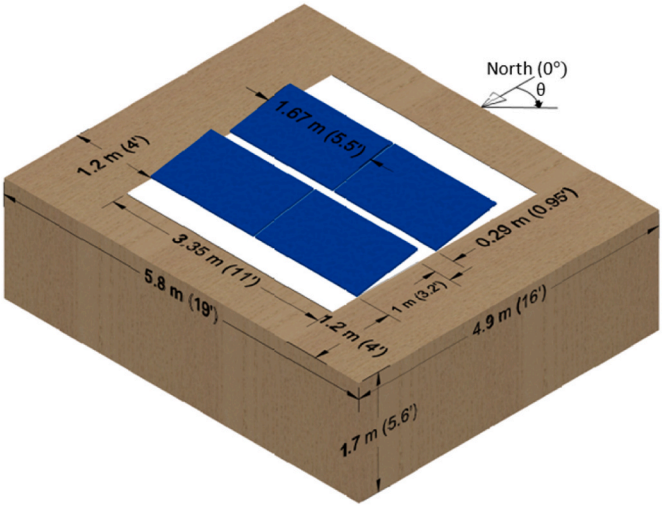

Fig. 2. Model configuration and dimensions.

nominally 10.16 cm × 20.32 cm × 40.64 cm (4" × 8" × 16″) concrete block that weighs 14.8 Kg (32.6 lbs) [see Fig. 4].

To conduct the aerodynamic rigid model testing, a set of four dummy panels that replicate the shape of the real PV panels were fabricated from plexiglass and plywood. These dummy panels were then instrumented with a total of 376 pressure taps, evenly distributed with 47 taps on the upper surface and 47 taps on the lower surface of each panel and secured to the racking system [see Fig. 5 (a)]. Pressure taps consisted of polyurethane tubes connected to a ZOC33/DSM4000 Scanivalve data acquisition system that collected pressure data for a 60-s duration and at a 520 HZ sampling frequency. In this study, the integral length scale of longitudinal turbulence was calculated to be 0.3 m. With a mean wind speed of 21.6 m/s used in the aerodynamic tests, the corresponding integral time scale is 0.014 s. The 60-s duration of the test is thus sufficient as per the ASCE 49 standard for wind tunnel experiments, which requires a minimum of five hundred longitudinal timescales to achieve stable pressure statistics (Wind tunnel testing for buildings, 2012). The collected data were then corrected using a tubing transfer function to account for the distortions created by the tubing length (Irwin et al., 1979). In addition, a total of five accelerometers placed at the bottom surface's center of each panel and on the NE support [see Fig. 5 (b)], were used to measure the system's wind-induced accelerations and consequently identify the dynamic properties (e.g., natural frequency and total damping ratio).

Fig. 1. Full-scale PV array in the WOW EF test section.

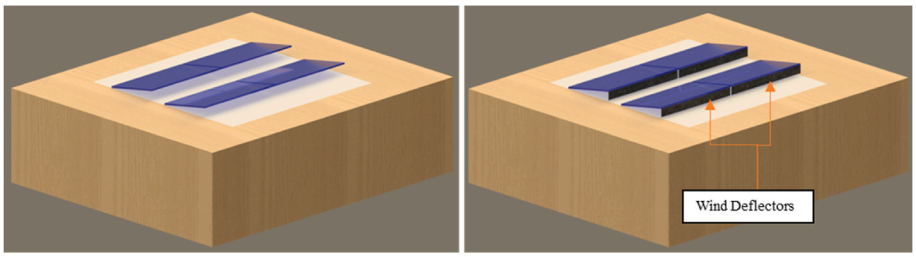

Fig. 3. PV panels (a) before and (b) after the addition of wind deflectors.

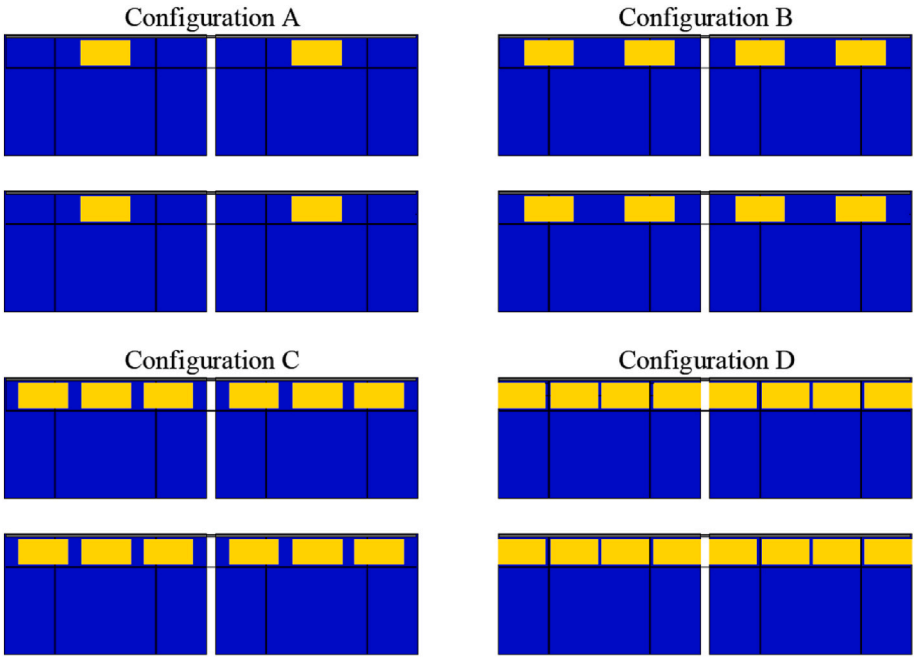

Fig. 4. PV ballast configuration.

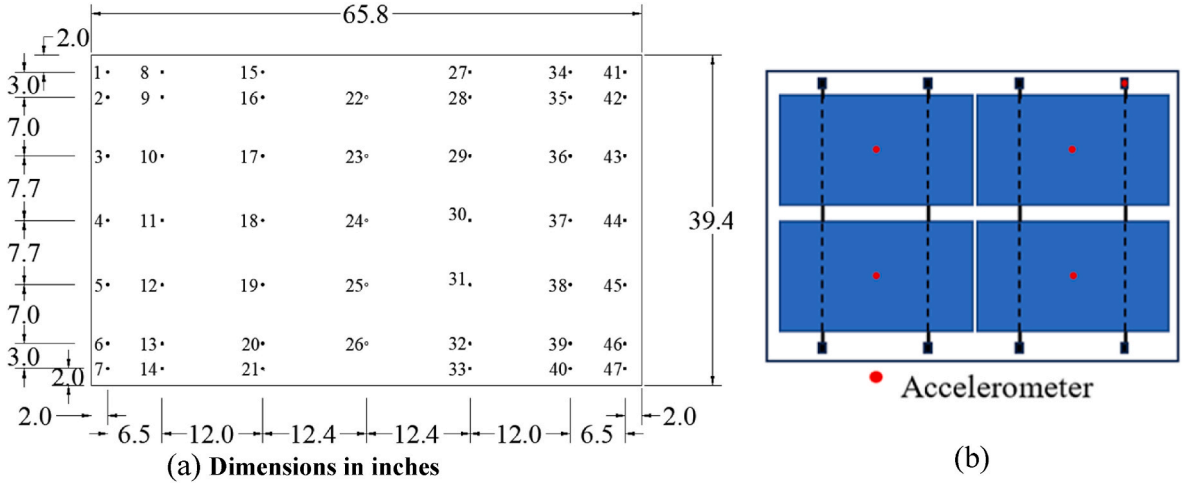

Fig. 5. Instrumentation layout: (a) pressure taps, and (b) accelerometers.

2.2. Wind flow simulation and testing protocol

The aerodynamic testing was conducted at a mean wind speed $\overline{U}_m$ = 22 m/s (49 mph) at the mean roof height h = 1.82 m (6 ft) under open terrain conditions with a roughness length Z_0 = 0.07 m (0.23 ft), classified as exposure C according to ASCE 7–22 (American Society of Civil Engineers). The tests were conducted in two phases for ballast Configuration C with and without the presence of wind deflectors. Specifically, the first phase was conducted for wind directions of 0°–180° at 10° increments, as well as 45° and 135°, whereas the second

phase consisted of wind directions from 0° to 90° at 10° increments, as well as 45°. Priority was given to testing most wind directions for the scenario with the wind deflectors as such deflectors are installed for majority of the ballasted PV applications in the real world. In addition to aerodynamic testing, a series of dynamic tests were conducted on the ballasted PV system. Similar to the aerodynamic tests, the first phase included wind directions of 0°–180° at 10° increments, as well 45° and 135°, for three mean wind speeds of 23.25 m/s (52 mph), 26.80 m/s (60 mph), and 30.4 m/s (68 mph), at the mean roof height *h*. The second phase consisted of testing the system without the wind deflectors at wind directions 0° and 45°.

High-speed failure assessment tests in dry and wet conditions were conducted at wind speeds starting from 18 m/s (40 mph) and increased by 3.6 m/s (8 mph) increments for all ballast configurations until the system's failure was observed. In addition, the performance of the ballasted PV system under wind-driven rain conditions was evaluated to understand the effect of a moist TPO membrane on the sliding wind speed of the system. The wind-driven rain capability of WOW EF features a full-scale raindrop size and hurricane-like simulated rain concentration. The raindrop size and rain concentration were validated against a model by Tokay et al. (2013), which uses three real hurricanes to match rain characteristics (Alawode et al., 2023), (Vutukuru et al., 2020).

Finally, to simulate the sliding resistance of a typical large rooftop ballasted array, and to investigate the uplift failure mode, the high-speed failure assessment test was conducted after mechanically fastening the leeward edge of the system to the roof to prevent sliding. For this specific case, the maximum capacity of 8 ballasts was used for NW, NE, and SE panels, while 4 ballasts were used for the SW panel, and the test was conducted for the most critical wind direction of 45°. The testing protocol is summarized in Table 1.

It is essential to ensure that the simulated flow conditions in the WOW match those of the atmospheric boundary layer. Turbulent Flow Instruments probes were used to measure free stream wind speeds at the center of the turntable for a 1-min duration. Fig. 6 (a) shows the mean wind speed and turbulence intensity profiles based on free-stream wind flow measurements, compared with those generated using ESDU item 85020 (ESDU (Engineering Sciences Data Unit), 2001) with a roughness length $z_0 = 0.07$ m.

It is to be noted that the tests were conducted in a partial turbulence simulation (PTS), hence the turbulence intensity and the integral length scale at the mean roof height of the model are smaller than those corresponding to the real-world Atmospheric Boundary Layer (ABL) representing the full turbulence spectrum. This mismatch is often encountered in large-scale and full-scale wind tunnel experiments due to the size limitation of the wind tunnel test section compared to the atmospheric boundary layer in nature (Asghari et al., 2016; Morrison and Kopp, 2018; Guo et al., 2021; Acosta et al., 2024).

Table 1
Test protocol.

Testing Type	Ballast Configuration	Wind Direction (deg)	Wind Speed (mph)
Aerodynamic	C	0:10:180 + 45 + 135	49
Aerodynamic (No Deflector)	C	0:10:90 + 45	49
Dynamic	C	0:10:180 + 45 + 135	52:8:68
Dynamic (No Deflector)	C	0 + 45	52:8:68
Destructive (Dry)	A	0	34:8:58
		45	34:8:58
		90	34:8:90
	B	0	34:8:66
		45	34:8:58
		90	34:8:98
	C	0	58:8:82
		45	58:8:76
		90	58:8:122
	MAX	45	58:8:103
Destructive (Wet)	A	45	42:8:58
	B	45	42:8:66
	C	45	42:8:74

The PTS methodology developed and validated at the WOW EF (Asghari et al., 2016), (Moravej, 2018), has been adopted successfully in large-scale and full-scale wind tunnel experiments and has been shown to produce wind effects comparable to field measurements (Alawode et al., 2023; Tolera et al., 2022; Estephan et al., 2021; Matus, 2018; Azzi et al., 2020a). Fig. 6 (b) shows the nondimensional WOW generated spectrum compared to the ABL von Karman spectrum; the mean roof height was used to normalize the frequency based on the recommendation of using turbulence-independent parameters that often masks the non-dimensional plots as shown by (Richards et al., 2007). The comparison clearly shows that the high frequency part of the turbulence spectrum was accurately simulated at the mean roof height of the model, which was previously proved to be necessary for the accurate simulation of flow separation, reattachment, and shear layers affecting local peak pressures (Kopp and Banks, 2012; Irwin, 2009; Tieleman, 2003; Melbourne, 1979; Richards et al., 2015). Hence, the simulated flow characteristics on the tested PV array align with real-world conditions, rendering the generated data and loads comparable to those experienced by actual PV arrays in the field.

On the other hand, the low-frequency content of the spectrum, accounting for the bulk of low-frequency larger eddies contributing to the integral length scale, are not fully simulated as expected in a partial turbulence simulation (PTS). Studies by (Asghari et al., 2016), (Yamada and Katsuchi, 2008; Sangchuwong et al., 2013; Katsuchi and Yamada, 2011) suggest that the corresponding turbulence intensity in PTS experiments should be determined from the following Equation (1) which accounts for the smaller integral length scale:

$$\frac{I_{um}}{I_{up}} = \left(\frac{{}^{x}L_{um}}{{}^{x}L_{up}}\right)^{1/3}\left(\frac{b_p}{b_m}\right)^{1/3} \quad (1)$$

For the experiments reported in the paper, Equation (1) yields the model turbulence intensity to be 7% which closely matches the turbulence intensity at the mean roof height of the model as shown in Fig. 6 (a). In the PTS method the effects of the missing low-frequency turbulence (as reflected in the lower turbulence intensity compared to that of ESDU's) on the wind-induced pressures are analytically compensated in the post-test analysis using a quasi-steady assumption. Such Partial Turbulence Simulation (PTS) method that separates the turbulence spectrum into two separate statistical processes – (i) the high frequency turbulence, accurately simulated in the experiments (see Fig. 6(b), and (ii) the low frequency turbulence treated as a quasi-steady process and compensated for analytically – has been shown to be effective and validated by several researchers including (Asghari et al., 2016), (Moravej, 2018; Wind tunnel testing for buildings, 2012; Kopp, 2023; Moravej et al., 2024; Enshaei et al., 2023). Hence, the PTS simulation adopted for this full-scale testing, and the corresponding flow parameters generated, can be considered adequate for the objective of this research.

It is important to note that while the effects of low-frequency turbulence on pressure coefficients can be analytically compensated for, they still pose a limitation in failure assessment tests, as they cannot be accounted for in that context.

It is worth mentioning that although the base building model dimensions differ from those of a full-scale commercial low-rise building due to size limitation of the test section, it is assumed to represent a corner of a larger building with the PV array situated on the roof's corner maintaining the 1.22 m (4′) minimum edge distance required by the code. Previous Wall of Wind studies also used a similar concept for full-scale and large-scale testing and yielded satisfactory results (Naeiji

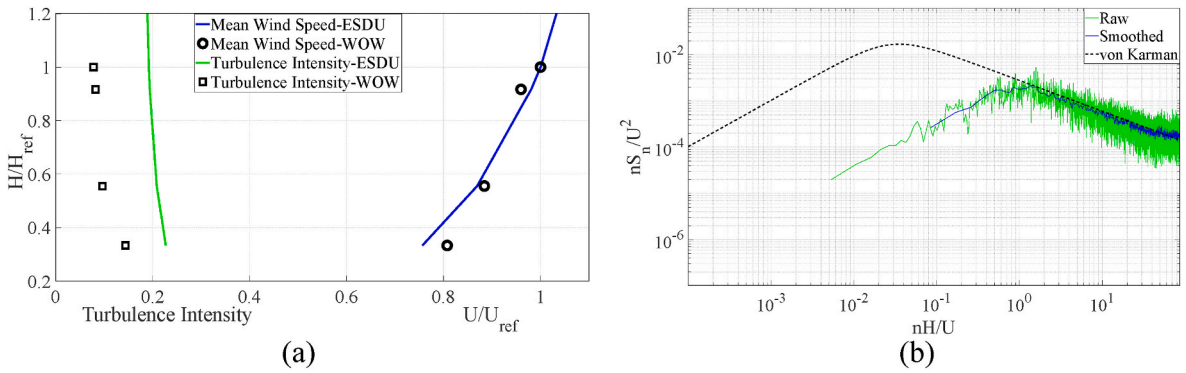

Fig. 6. (a) Open terrain wind speed and turbulence intensity profiles and (b) Normalized PSD of the longitudinal velocity fluctuations.

et al., 1868), (Alawode et al., 2023; Tolera et al., 2022; Estephan et al., 2021; Matus, 2018; Azzi et al., 2020a).

2.3. Data analysis

Wind-induced pressure data for each pressure tap on the upper and lower surfaces of the dummy panels were collected for the tested wind directions. Instantaneous net pressure coefficients (C_p) were calculated from the raw pressure data using Equation (2), where $\Delta P(\theta,t)$ is the pressure difference between the upper surface tap and lower surface tap in psf, ρ is the air density in kg/m^3 (slugs/ft^3), θ is the wind azimuth in degrees, and $\overline{U}$ is the mean wind speed at the mean roof height in m/s (ft/s). Consequently, mean and peak pressure coefficients ($\overline{C}_p$ *and* $\widehat{C}_p$) were computed using Equations (3) and (4), respectively. Note that for the context of this paper, negative pressures are those acting away from the PV panel's surface (suction), while positive pressures are those acting towards the panel's surface.

The PTS method, described briefly in Section 2.2, was used to analytically compensate for the effects of the low-frequency turbulence deficit in the measured wind flow fluctuations.

Each pressure time history for the test duration (mentioned in Section 2.1) was divided into subintervals. Two aspects need to be carefully considered – (i) the length of each subinterval and (ii) the total number of subintervals. Firstly, each subinterval needs to be long enough to be treated as an independent gust event. Secondly, Moravej (2018) conducted a sensitivity analysis on the impact of the number of subintervals on the generated peak pressures and found that peak values stabilize when the number of subintervals reaches 100 or more. The probability that the peak pressure coefficient within a subinterval will remain below a certain value is fitted using a Fisher-Tippet Type I distribution. Given that turbulence in a generic boundary layer follows a Gaussian distribution, the missing large-scale turbulence is assumed to have a Gaussian distribution in the PTS method. The expected peak pressure coefficients are calculated by combining the joint probabilities of the measured pressure coefficients in the physical experiments (accounting for the high-frequency turbulence) and the assumed Gaussian distribution for the missing low-frequency turbulence.

For the current data analysis, the pressure coefficient time series was divided into 100 sub-intervals, each lasting 0.6 s. This duration, being longer than the gust duration of 0.325 s, ensures that the sub-intervals remain independent. Then, $\widehat{C}_p$ were estimated using the Fisher Tippet Type I fit extreme value analysis for a 1-h storm duration (at full scale). The turbulence intensity of the missing low-frequency turbulence was $I_{UL} = 18.33\,\%$, the target probability of non-exceedance was $P_N = 0.78$ for the 1-h duration, and the exceedance probability per subinterval was $G = 4.455 \times 10^{-5}$. To compare with ASCE 7–22, the $\widehat{C}_p$ values were normalized by the 3-s gust wind speed $\widehat{U}_{3s}$ which was obtained using Equation (5) where $\overline{U}_{3600s}$ is the mean hourly wind speed. Moreover, the area-averaged pressure coefficient time series, or force coefficients $C_F(\theta,t)$ were computed using Equation (6). Additionally, the correlation coefficients (C_C) between pressures at different points were calculated using Equation (7) where X' denotes the fluctuating component of the time history (X' = X − $\overline{X}$), and the bar denotes the temporal average (Holmes, 2015)

$$C_P(\theta,t) = \frac{\Delta P(\theta,t)}{\frac{1}{2}\rho\overline{U}^2} \tag{2}$$

$$\overline{C}_p(\theta) = \frac{\overline{\Delta P}(\theta)}{\frac{1}{2}\rho\overline{U}^2} \tag{3}$$

$$\widehat{C}_p(\theta) = \frac{\widehat{\Delta P}(\theta)}{\frac{1}{2}\rho\overline{U}^2} \tag{4}$$

$$\frac{\widehat{U}_{3s}}{\overline{U}_{3600s}} = 1 + 3.4\,I_U \tag{5}$$

$$C_F(\theta,t) = \frac{\Sigma_i \Delta P_i(\theta,t).A_i}{\frac{1}{2}\rho\overline{U}^2.\Sigma_i A_i} \tag{6}$$

$$C_C = \frac{\overline{X'_1 X'_2}}{\sigma_{X_1}\sigma_{X_2}} \tag{7}$$

The advanced PTS method, developed by Estephan et al. (2022) and validated using field measurements on full-scale rooftop PV array on a low-rise building at the Central Washinton University (CWU) (Estephan, 2022), was used to analytically incorporate the effects of both the low-frequency turbulence deficit and dynamic response of the structure in the measured force coefficient time history $C_F(\theta,t)$. This method uses the mechanical admittance function $|H(f)|^2$ presented in Equation (8) to compensate for the resonant component in the wind loading spectrum, along with the gust transfer function $|T(f)|^2$ presented in Equation (9) to incorporate the effects of the missing low-frequency turbulence (Banks et al., 2015). The advanced PTS method generates the full compensated wind loading force coefficient time history $C_{F(B+R)}(t)$ which includes both the background (B) and resonant (R) components, and it is obtained from the compensated spectrum using Inverse Fast Fourier Transform (IFFT) (Estephan et al., 2022). The dynamic amplification factor, which is the ratio of $\widehat{C}_{F(B+R)}$ to $\widehat{C}_{F(B)}$, was then calculated for varying wind speeds [see Equation (10)]. $\widehat{C}_{F(B+R)}$ is the peak force coefficient which includes the background and the resonant components and $\widehat{C}_{F(B)}$ is the peak force coefficient which includes the background component only.

$$|H(f)^2| = \frac{1}{\left[1 - \left(\frac{f}{f_n}\right)^2\right]^2 + 4\,\zeta^2\left(\frac{f}{f_n}\right)^2} \tag{8}$$

$$|T(f)|^2 = \frac{S_{u,FS}(f)}{S_{u,PS}(f)} = \frac{S_{C_F(B),FS}(f)}{S_{C_F(B),PS}(f)} \tag{9}$$

$$DAF = \frac{\widehat{C}_{F(B+R)}}{\widehat{C}_{F(B)}} \tag{10}$$

3. Results and discussion

This section presents the outcomes of the experimental testing. Subsection 3.1 discusses the effect of the wind direction and wind deflectors on the spatial distribution of aerodynamic pressure coefficients. Section 3.2 assesses the influence of deflectors on the top and bottom force coefficients for each of the four panels. Subsection 3.3 evaluates the effect of wind deflectors on the power spectral densities of individual and area averaged time histories. Subsection 3.4 compares the peak force coefficients before and after the addition of wind deflectors with the ASCE 7 envelope for roof mounted arrays. Subsection 3.5 evaluates the effect of wind deflectors on the correlation coefficients between net pressure time histories. Subsection 3.6 addresses the wind induced dynamic effects and the amplification of wind loading on the array. Finally, subsection 3.7 discusses the high-speed failure assessment results and failure wind speeds.

3.1. Spatial distribution of pressure coefficients

3.1.1. Mean net pressure coefficients

A comparison of the spatial distribution of mean net pressure coefficients $\overline{C}_P$ over the four PV panels before and after the addition of wind deflectors is presented in Fig. 7 (a), (b), and (c) for wind directions 0° referred to as normal wind, 45° referred to as cornering wind, and 90° referred to as side wind respectively. For the sake of brevity, only these cases were selected to discuss the aerodynamics of the array for these three main wind directions. Before the addition of wind deflectors, the wind loading on the system was due to flow separation over the structure's bluff body, as well as local flow separations on the array edges. For the case of normal wind ($\theta = 0°$), the loading was observed to be symmetric across the east and west panels, with negligible differences that likely arise due to the bundling of pressure tubing. Peak suctions were observed at the upper edges of the four panels due to flow separation at those edges where the minimum value (i.e., maximum suction) was $\overline{C}_p = -0.7$ on the top edge of the NE panel. The wind loads were observed to decrease gradually as the distance from the edges increased due to the local array flow reattachment. For cornering winds ($\theta = 45°$), the peak suctions were at the upwind corner and corresponding leading edges of the NE panel [$\overline{C}_p = -3.0$] as shown in Fig. 7 (b), followed by the upwind corner of the SE panel [$\overline{C}_p = -2.7$]. This is due to the formation of local conical vortices along the upwind corners of the panels. The observed suctions decrease gradually within the same panel which indicates a reduced intensity of the conical vortices as the distances from the upwind corners increase, aligning with the observations of Banks (2013). This is not the case for NW and SW panels where $\overline{C}_p$ values are significantly lower than the windward panels (60% lower) except at the windward corner of the SW panel where $\overline{C}_p = -1.9$. This can be attributed to the shielding effect that the windward panels, which are exposed to direct cornering winds, have on the leeward panels. It is noteworthy to point out that for cornering winds, the western edge of the NW panel (where the effects of conical vortices faded), encountered reduced loads compared to loads under normal wind directions. This observation suggests that, while cornering winds impose substantial wind loads on corner modules, they might not be the primary concern for edge modules, as normal winds remain the more critical direction for them.

As for the case of side wind ($\theta = 90°$), it is evident that pressure equalization is almost achieved due to the improved aerodynamic shape of the system for this specific wind direction. The reduced flow disruption results in similar flow characteristics for the top and bottom surfaces, consequently generating almost equal suctions, leading to a net load of zero on the array. Moreover, analysis of the top surface suction showed that flow reattachment is evident at a distance of 3.8 m (12.5′) from the building's windward edge where the suction reduces to zero.

The addition of wind deflectors to the system had a significant impact on the wind loading for cornering wind directions and a negligible effect for normal and side winds. Considering the normal wind first [Fig. 7 (a)], the addition of wind deflectors did not alter the pressure distribution across the array, which was almost identical to the case where no deflectors were added. This phenomenon may be a function of the proximity of the system to the edge of the building. Considering the flow reattachment length described in the previous section (3.8 m, 12.5′) and given that the distance from the building edge to the leeward extremity of the array for normal wind is 3.45 m (11.33'), this positions the entire system under the separation bubble for this specific wind direction. This may explain the ineffectiveness of wind deflectors for this case. To gain more insights, additional research is needed to examine how the system behaves when exposed to a fully attached flow, in order to compare and quantify the impact of deflectors.

As for cornering winds ($\theta = 45°$), the addition of wind deflectors resulted in a significant drop in the magnitude of the suction on the array [see Fig. 7 (b)]. The decrease of the surface suction was in the order of 50%, especially on the windward corners of the east windward panels. However, no variations were noted after comparing the loads on the NW panel before and after the addition of deflectors. This shows that the mitigation effect of wind deflectors is most efficient for corner modules. This efficiency is reduced for edge and interior modules.

Finally, as shown in Fig. 7 (c), the distribution of pressure coefficients for ($\theta = 90°$) wind direction wasn't altered after the addition of wind deflectors. The reason behind that is that the wind deflectors in this experiment are only fitted to the back of the modules and not to the sides, so for this specific wind direction, the frontal area of the system was not altered after adding deflectors.

3.1.2. Peak net pressure coefficients

In addition to the mean pressure coefficients, the comparison of the distribution of the worst peak net pressure coefficients generated by the PTS method (in terms of $\widehat{C}_{p\ 3\ sec}$) from wind directions [0: 90°] are presented in Fig. 8 for an array with and without wind deflectors. The critical peak suction values at the corners of the NE and SE panels are shown to be greatly reduced after the addition of wind deflectors (50% reduction). However, consistent with the mean pressure distribution results, the addition of wind deflectors did not have a significant impact on the magnitude of peak pressures, apart from the windward corners of the two windward panels (NE and SE). Further, the distribution shows that even for the top-left edge of the windward panels (NE and SE), the magnitude of the peak pressures is almost the same as the case without wind deflectors. This further emphasizes the previous discussion that the mitigation effect of wind deflectors is most efficient for the corner panels only. Moreover, the difference between mean and peak values was noticed to be significant for all angles; this indicates the high fluctuating nature of the incoming turbulent flow due to both global and local flow separations at the edges of the building and at the edges of the array, respectively

3.2. Force coefficients considering each panel

Further analyses were performed on the aerodynamic data on each the of the four panels to investigate the effect of the deflectors on the

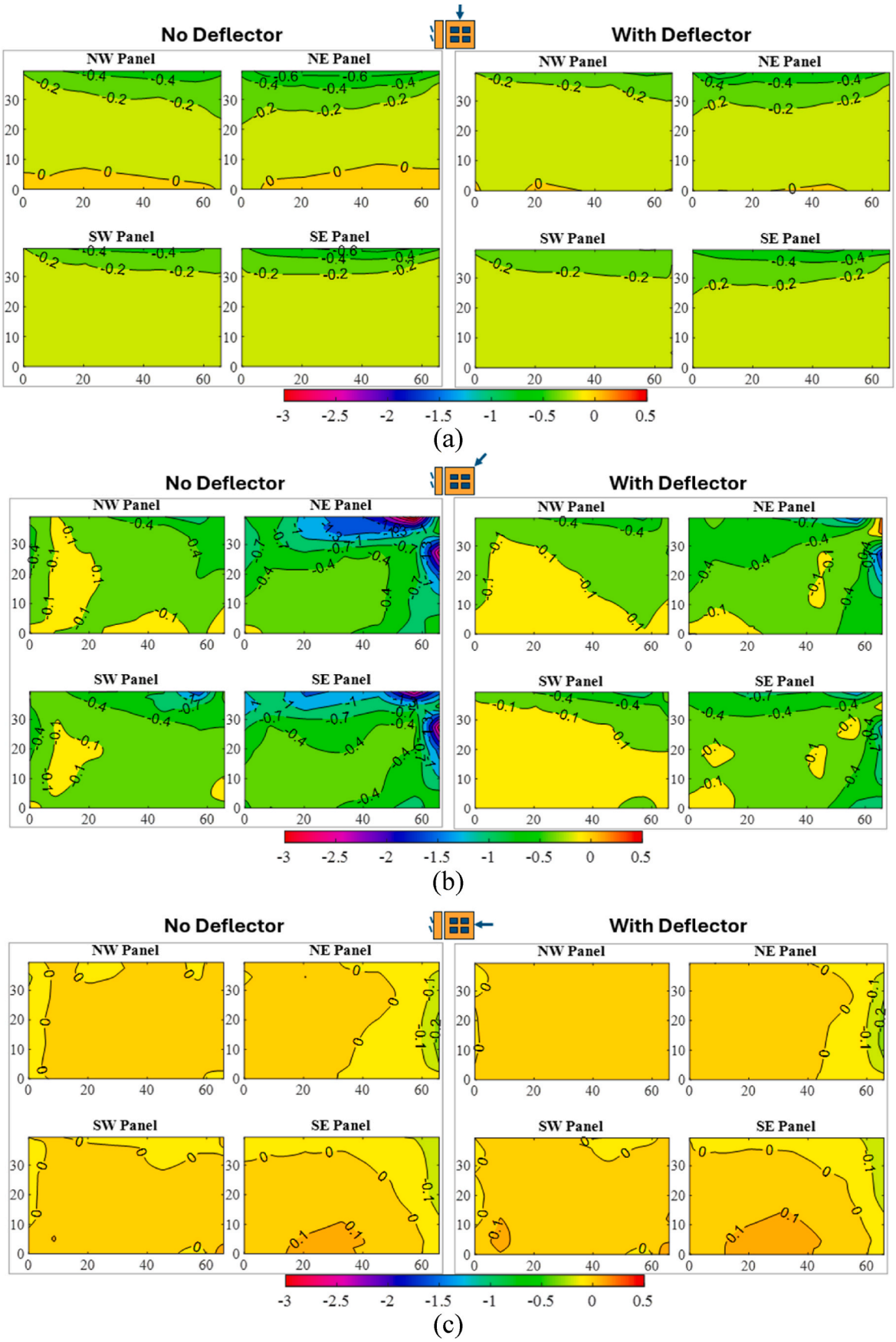

Fig. 7. Comparison of the spatial distribution of mean net pressure coefficients $(\overline{C_p})$ over the array before and after the addition of wind deflectors for (a) $\theta = 0^\circ$, (b) $\theta = 45^\circ$, and (c) $\theta = 90^\circ$ wind directions.

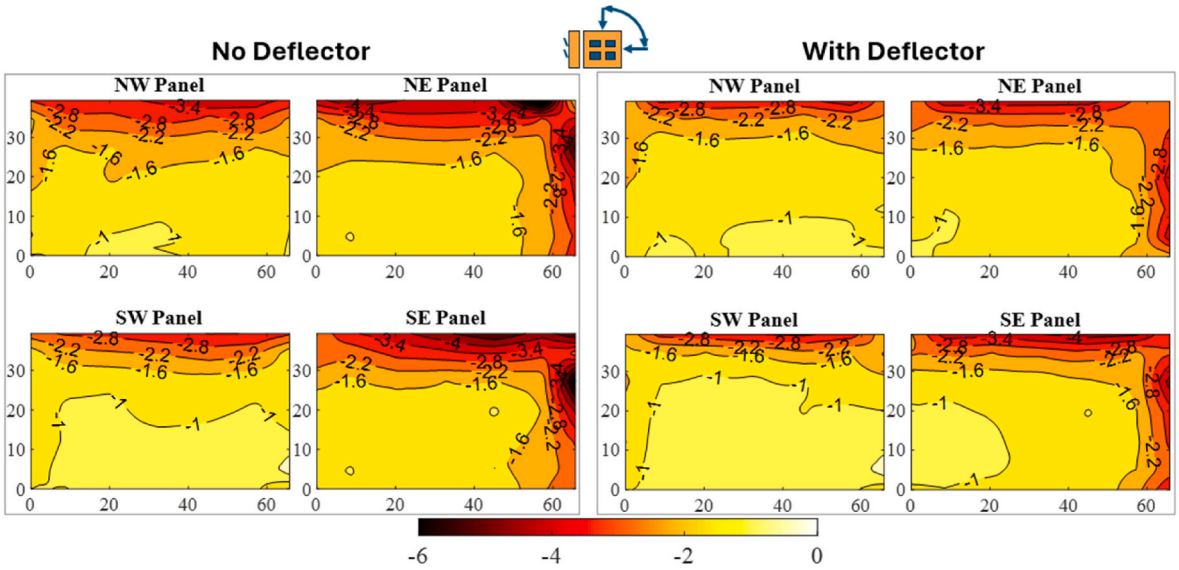

Fig. 8. Comparison of the spatial distribution of peak net pressure coefficients $\widehat{C}_{P\ 3\ sec}$ before and after the addition of wind deflectors.

force coefficients averaged for each panel's full area. Figs. 9 and 10 show the mean and peak top, bottom, and net force coefficients for the four panels as a function of wind direction for the two cases: (1) with wind deflectors and (2) without wind deflectors.

The mean and peak coefficients plots were observed to exhibit a similar behavior. The $\overline{C}_F$ plots in Fig. 9, show negative coefficients on the top surface as expected. However, for the bottom surface coefficients, especially for the case without wind deflectors, positive values were observed. These positive pressures occur in the cavity between the roof and the panels, and they correspond to pressures that try to lift the panels off the roof. An increase in pressure on the bottom surface indicates an increase in the upward force exerted on the panels, while a decrease in this pressure suggests a favorable reduction in the upward force.

When combined with the negative top pressures that attempt to pull the panels upward, these positive bottom pressures create a worst-case scenario by increasing the net uplift on the panels. Conversely, when the pressure values on the bottom surface of the panels are negative, the resulting negative pressure attempts to pull the panels downwards, adding to the stabilizing force provided by the ballast and array weight. Hence, creating a favorable scenario and reducing the net uplift on the panels, even when accompanied by negative top surface pressures. An evident reduction in the overall $\overline{C}_F$ on the bottom surface for all the four panels was observed when a deflector is added. This drop implies a drop in the cavity pressure, and consequently a decrease in the net uplift on the array. The reduction was most pronounced for cornering wind di-

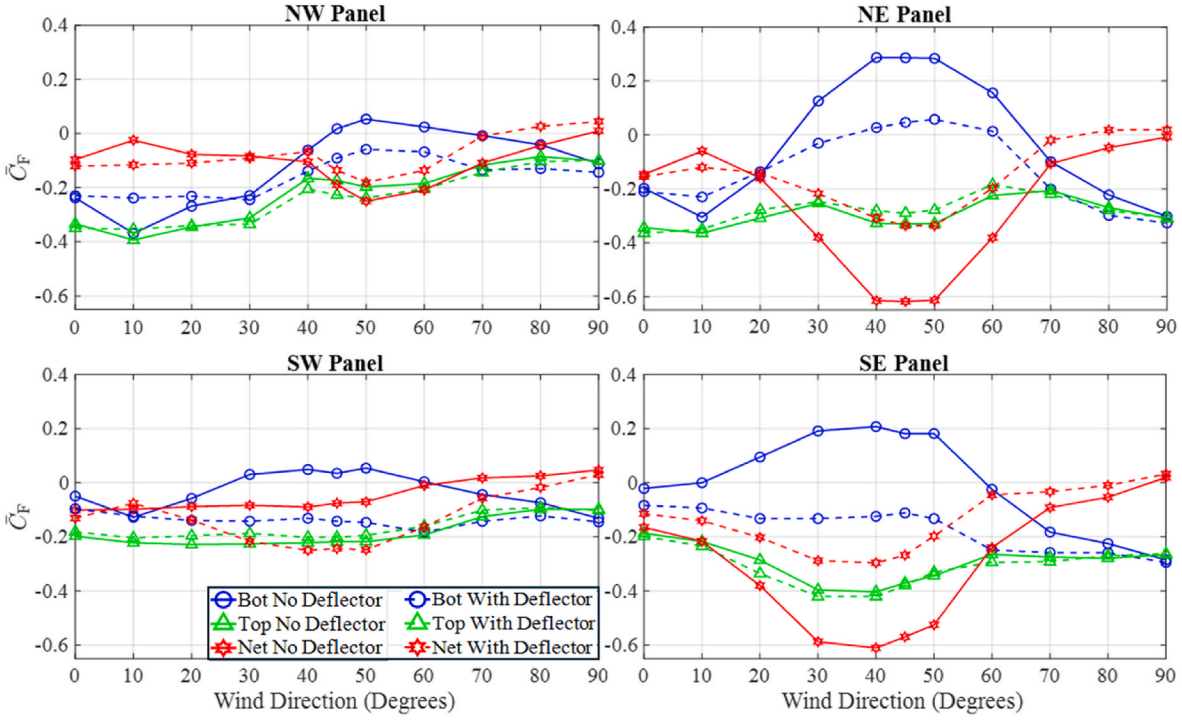

Fig. 9. Top, bottom, and net mean force coefficients $\overline{C}_F$ on the (a) NW, (b) NE, (c) SW, and (d) SE panels.

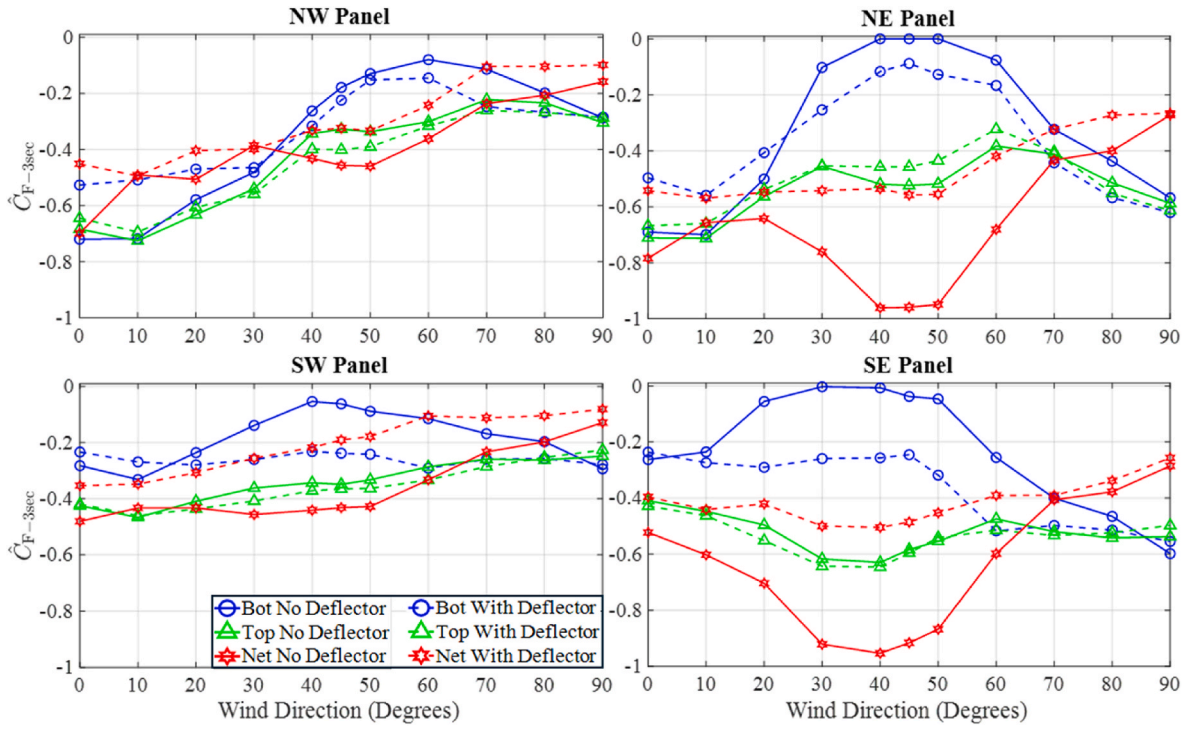

Fig. 10. Top, bottom, and net peak force coefficients $\widehat{C}_F$ on the (a) NW, (b) NE, (c) SW, and (d) SE panels.

rections where positive mean pressures on the bottom surface of the panels (acting upwards) were changed into desirable suctions pulling the panels downwards.

This observation was also noted for the $\widehat{C}_F$ plots in Fig. 10. However, instead of positive bottom surface pressures that push the panels off the roof, near-zero bottom surface pressures were observed in some cases especially for cornering wind directions for the NE and SE panels ($\theta = 30^\circ - 60^\circ$). Although the near-zero peak pressures did not create a worst-case scenario by amplifying the net uplift, they did not assist in stabilizing the panels on the roof along with the force of ballast and array weight as well. The addition of wind deflectors helped turn the near-zero bottom surface values observed for cornering wind directions into favorable negative values as well. In contrast, the mean and peak pressures on the bottom surface of the panels were noticed to increase after adding wind deflectors for ($\theta = 0^\circ, 10^\circ,$ and 20°) wind directions, leading to an increase in the net uplift. This explains the observations in the previous sections where no mitigation effects were noticed for these particular wind directions.

As for the net uplift, the reduction in mean and peak force coefficients is most prominent for the eastern panels when subjected to cornering wind directions where the addition of deflectors reduces mean and peak net uplift on these panels by the order of 50%. This reduction gradually decreases to zero for normal and side winds. In contrast, the mitigation effect is significantly less prominent for the western panels (NW and SW) even for cornering winds.

For the 90° wind direction, all the force coefficients were not altered, as discussed previously, because the deflectors have a minimal effect on the frontal area of the system in this specific case. While the addition of extra wind deflectors covering the entire array perimeter could potentially decrease the overall loading, it is considered unnecessary due to pressure equalization that already diminishes the net load on the system in this specific direction.

It is worth mentioning that the values of the mean and peak top force coefficients for all wind directions were shown to be almost unaffected by the addition of wind deflectors. The mentioned observations suggest that wind deflectors fitted to the back of solar panels mounted on flat roofs do not alter the top surface pressure distribution. The reduction in the net uplift that the deflectors introduce is a result of reducing the pressure values on the bottom surface of the panels. Moreover, the efficiency of the mitigation of these deflectors drops significantly for normal winds and as the distance from the array corners increases (i.e., for interior and edge panels).

This full-scale experimental test enables the accurate measurement of the aforementioned variations in cavity pressures resulting from the high Reynolds number of the flow, which is essential for correctly simulating real flow conditions inside cavities.

3.3. *Effect of wind deflectors on power spectral densities*

Based on the insights gained from earlier sections, it is evident that wind deflectors exhibit peak mitigation efficiency for cornering wind directions (30°–60°). To delve into the impact of wind deflectors on the pressure fluctuations across the panels, locations and power spectral densities of 8 selected net pressure time histories on the most critical NE panel are presented in Fig. 11 for the 45-degree wind direction.

As stated in Section 3.1, strong conical vortices form at the windward corners and gradually dissipate as the distance from the corner increases. To capture the effects of deflectors on the formation and dissipation of these vortices, taps 8, 22, and 34 were selected along the elevated edge of the NE panel at varying distances from the windward corner, with tap 34 being the closest, followed by 22, then 8. Similarly, taps 43 and 45 were selected on the east edge of the panel. Additionally, taps 29, 24, and 19 were selected as internal taps at varying distances from the NE edge to evaluate the deflector effects on the internal regions of the panels as well.

It is concluded from Fig. 7 (b) and 8 that taps 34 and 43 are located in the panel zone where the influence of conical vortices is highest, followed by taps 22 and 45. This is a known fact due to their proximity to the panel corner, in contrast to taps 8, 29, 24, and 19 where the effect of conical vortices is less pronounced.

It is well established that the area under the dimensional PSD plot is equal to the variance of the plotted time history (square of the RMS value) (Azzi et al., 2020a). This information is portrayed in Fig. 11

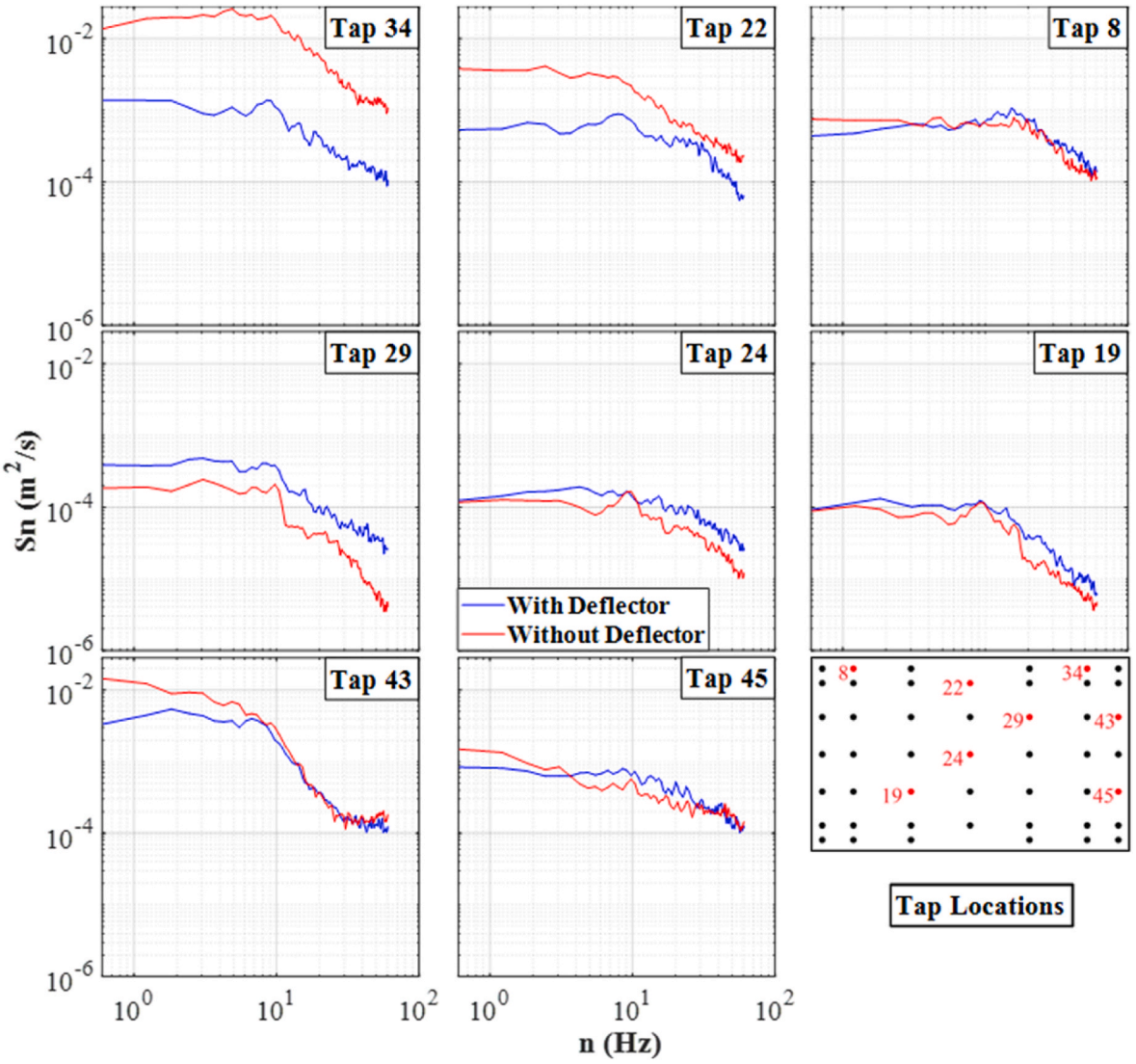

Fig. 11. PSD of taps 8, 19, 22, 24, 29, 34, 43, 45.

where, as expected, the PSD values are the highest for tap 34. The dissipation of conical vortices along the north edge of the panel is also portrayed in the figure where the PSD values gradually drop, moving from tap to 34 to 22, and finally 8. A similar dissipation pattern is noticed on the east edge as well. As for the internal taps, the PSD values for the internal taps are significantly smaller than those of the edge taps. Hence, it can be concluded that since the corners and edges of the panels experience more violent pressure fluctuations than the remaining areas, the PSD values in these areas are higher and consequently RMS of the pressure time histories.

The role of wind deflectors is evident in reducing the PSD values. Although all the taps show a reduction in PSD values, the most prominent reduction was for tap 34 where the PSD was reduced by almost 95%. The efficiency of this mitigation is noted to decrease moving away from the windward corner where even a slight reverse effect was noticed for taps 19, 45 and 8, especially at higher frequencies. These observations align with the discussions in the previous sections where pressure reductions were most effective on the windward corners of the panels. In summary, wind deflectors are most effective in mitigating pressure fluctuations in regions dominated by conical vortices. However, their efficiency diminishes in areas where the influence of these vortices is less pronounced.

3.4. Area averaged coefficients

Since wind loading varies across different sections of the tested array, an evaluation of the area-averaged loads of the array was conducted. The area-averaged peak net force coefficients for all wind directions $\widehat{C}_{F\,3\,sec}(\theta)$ were obtained for every combination of areas across the array adding up to 11015 area combinations which range from 0.012 m^2 (0.128 ft^2) to 6.69 m^2 (72 ft^2). It must be noted that the $\widehat{C}_{F\,3\,sec}(\theta)$ data was compensated for low frequency turbulence using the PTS approach discussed earlier. The worst force coefficient for all wind directions and for each area combination ($\widehat{C}_{F\,3\,sec}$) were plotted against the normalized wind area as per ASCE 7–22 and presented Fig. 12 without the wind deflectors and Fig. 13 with the wind deflectors. For this analysis, the panels are considered to act as a single system due to the effect of load sharing that occurs in the racking system that connects all the panels.

As per ASCE 7–22 section 29.4-7, the tested array lies in zone 3 of the building roof plan. Hence, the ASCE 7–22 envelope for rooftop solar panels in zone 3 is plotted in Figs. 12 and 13 for the sake of comparison with the results of this study. It is observed from Fig. 12 that the ASCE envelope can be considered conservative for the design of rooftop solar panels, where the $\widehat{C}_{F\,3\,sec}$ values although close, are still below the

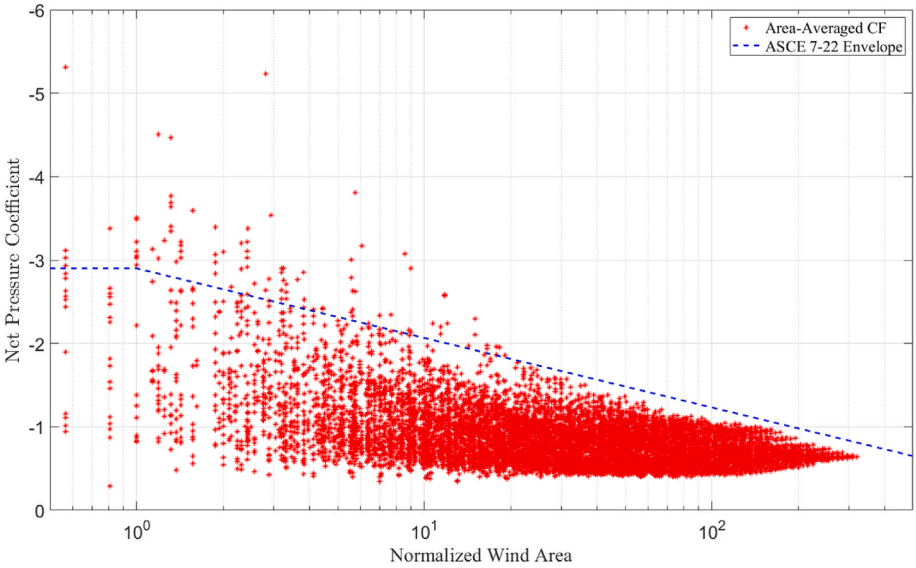

Fig. 12. Area-Averaged $\widehat{C}_{F\ 3\ sec}$ before the addition of wind deflectors.

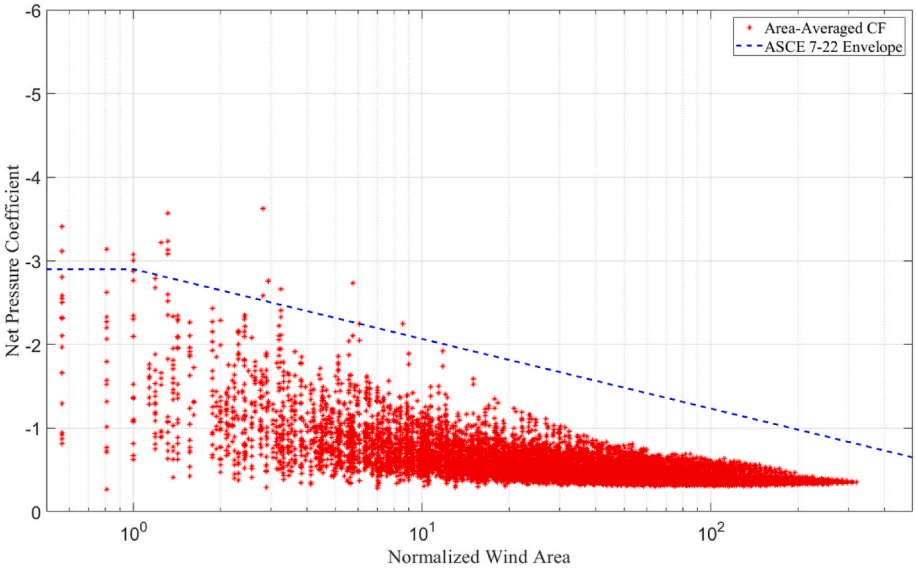

Fig. 13. Area-Averaged $\widehat{C}_{F\ 3\ sec}$ after the addition of wind deflectors.

envelope line. However, for smaller areas, a considerable number of outlying values were observed to exceed the ASCE envelope. For the case of ballasted PV systems, the absence of a mechanical connection to the roof renders these values critical. Excessive wind loading, even on a smaller area, may cause a significant lift in one or more of the supports of the array. This can create a cavity for wind to get underneath the system, leading to a sudden disruption of the aerodynamic behavior of the modules in proximity to the lift. Consequently, this may trigger a chain reaction where neighboring panels are also lifted and could potentially be flipped off the roof. The risk of support lifting is further increased due to the dynamic effects which this paper will address in the next section. The values of $\widehat{C}_{F\ 3\ sec}$ experienced a remarkable drop after adding wind deflectors to the system, as revealed in Fig. 13.

It was observed that the most critical negative $\widehat{C}_{F\ 3\ sec}$ dropped from -5.31 to -3.63, and the $\widehat{C}_{F\ 3\ sec}$ value for the total full area dropped by almost 50% from -0.64 -0.35 after the addition of wind deflectors. Moreover, the number of outlying values substantially decreased as well.

This indicates that deflectors play a significant role in mitigating wind loading from the most critical wind direction. However, according to conclusions from the previous sections, the efficiency of this mitigation is dependent on the wind direction. This conclusion is reflected in Fig. 14, where the variation of mitigation efficiency, represented by $\widehat{C}_{F\ 3\ sec}$ for the for the total array area as a function of wind direction, is evident. The efficiency of deflector is highest (50%) for $\theta = 45^{\circ}$ wind direction and decreases gradually as we move away from cornering winds. The efficiency also varies for each panel as previously pointed out in section 3.2. The reduction of design wind loads due to the application of wind deflectors needs further investigation as the deflectors can be possibly deformed or damaged at lower than the design wind speeds. Further research is deemed necessary to optimize the configurations and reliability of wind deflectors for enhanced mitigation effects.

3.5. *Effect of wind deflectors on correlation coefficients*

The correlation coefficient between two-time dependent variables is

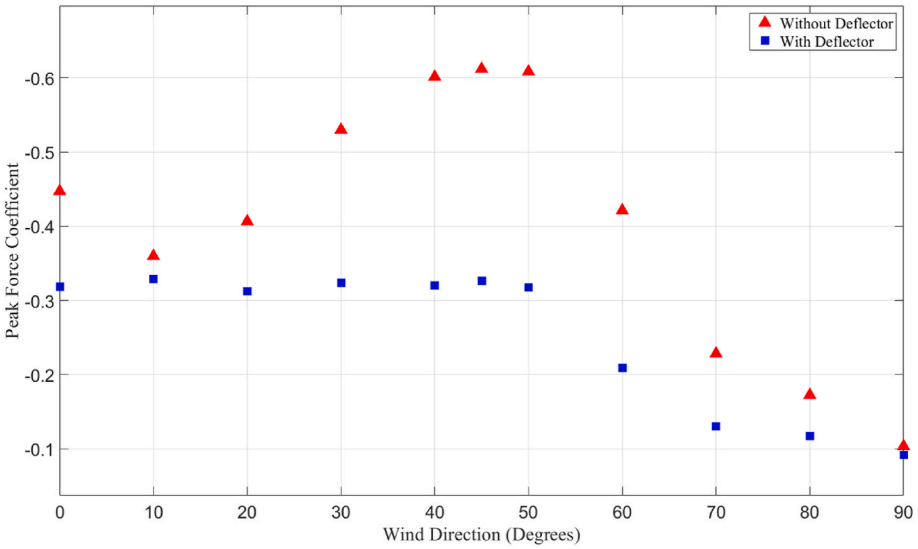

Fig. 14. Peak force coefficients $\widehat{C}_{F\ 3\ sec}$ for the total array area.

a value that ranges between −1 and 1. A correlation coefficient of 1 implies perfect positive correlation (signals are in-phase) and −1 implies a perfect negative correlation (signals are out of phase). A correlation coefficient of 0 implies a complete absence of correlation (Holmes, 2015).

This section tackles the effect of the addition of wind deflectors on the correlation coefficients between the instantaneous aerodynamic pressures on the most critical NE panel. In this section, the net time histories of the pressure taps are addressed (top – bottom). This investigation is important since high correlation between pressure taps implies that the corresponding tributary area experiences similar peaks in wind loading, increasing the likelihood of elevated area averaged pressures. For this task, the correlation coefficient C_C was calculated between the net time histories of the pressure taps of the NE panel with respect to taps 29 and 34 [see Fig. 11] before and after the addition of wind deflectors. The evaluated pressure taps were chosen such that one is located on the corner (tap 34) where the effects of corner vortices are prominent, and the other is an internal tap to investigate the reduction in correlation on the internal zone of the PV panel as well (tap 29). The results are plotted in Fig. 15 for tap 34, and Fig. 16 for tap 29.

The results show a notable decrease in correlation coefficients after the installation of wind deflectors for both edge and internal taps. Interestingly, the reduction in correlation is not only limited to pressure taps in proximity to the selected taps but extends beyond adjacent taps to the entire set of pressure taps on the NE panel as shown in Fig. 15. This is clearly portrayed in Fig. 16 as well, which shows a noticeable

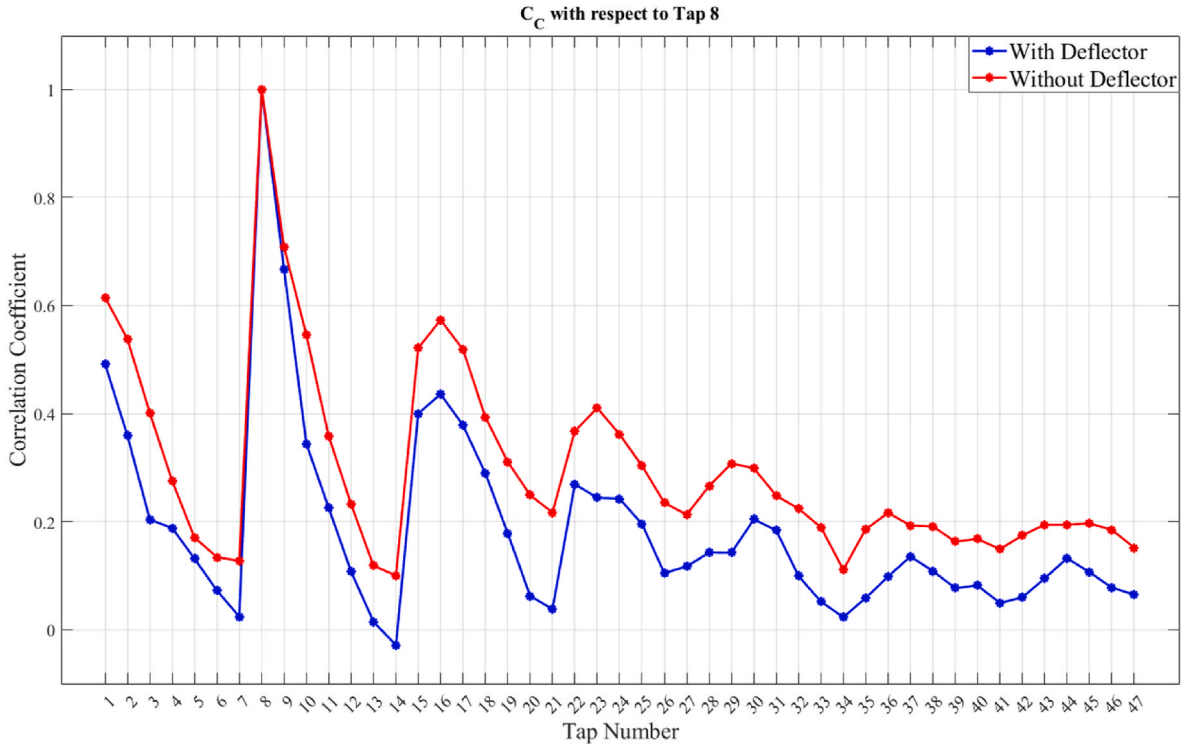

Fig. 15. Correlation coefficient of all the pressure taps on the NE panel with respect to tap 34.

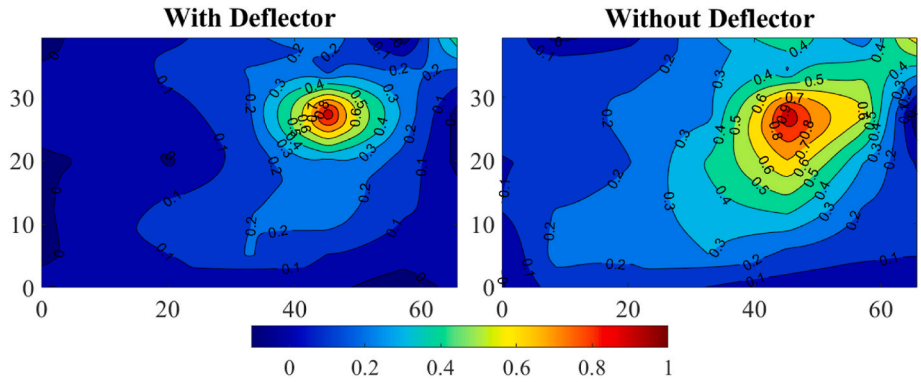

Fig. 16. Spatial distribution of the correlation coefficient of all the pressure taps on the NE panel with respect to tap 29.

reduction of the correlated area. Initially encompassing most of the NE panel, the correlated area was observed to shrink by around 80% from 0.516 m^2 (5.55 ft^2) to 0.11 m^2 (1.18 ft^2) after the addition of deflectors, a small area comprising adjacent pressure taps only.

For this experiment, the inclusion of flexible wind deflectors seems to induce localized effects that break the correlation among pressure taps on the panels. One possible cause of this correlation drop might be the disruption of the formation and transport of vortices forming due to local flow separation on the windward edges and corners of the panels. In-depth flow analyses such as Particle Image Velocimetry (PIV) are required for a precise scientific understanding of how wind deflectors influence the flow structure over roof mounted solar panels. These results can only be captured using large and full-scale testing, highlighting the limitations of traditional small-scale wind tunnel tests employing rigid models.

This drop in correlation justifies the significant reduction in area averaged coefficients discussed in section 3.4. Although the results of section 3.1 revealed that the addition of wind deflectors was observed to be inefficient in reducing peak pressures for individual pressure taps under normal winds, and section 3.3 showed that deflectors did not reduce the pressure fluctuations for pressure taps that are not in the proximity of the windward corners, the findings of this section suggest that wind deflectors effectively alter wind loading patterns on the panels. This modification prevents simultaneous peak loading on adjacent areas, thereby resulting in a reduction in the area averaged pressure and consequently the net uplift on the array.

3.6. Wind induced dynamic effects

Studying the wind induced dynamic effects on PV arrays is essential to develop reliable design methods. In this section, the wind induced dynamic effects are accounted for in post-test analysis using the advanced PTS method (Estephan et al., 2022). This method uses the natural frequency of the system (f_n), the total damping (ζ), and the full-scale parameters of the prototype as inputs to generate the complete wind loading spectrum, incorporating the effects of the missing low-frequency turbulence and including the resonant effects. The natural frequency and damping ratio were obtained by applying the Random Decrement (RD) technique (Tamura and Suganuma, 1996), (Jeary, 1992) to the acceleration time histories which incorporate the resonant response. This technique utilizes a time-domain approach wherein the structural responses to specific operational loads of a given structure are converted into random decrement functions. The obtained parameters from the RD technique were $f_n = 11.5$ Hz and $\zeta = 3\%$. The damping value may change according to the accelerometer's position on the racking system. In this study, the damping is calculated based on the acceleration data obtained from the accelerometers placed on the centers of the panels.

Additionally, Fig. 17 shows the acceleration power spectra for the five accelerometers used to capture the vibrations of each of the four modules. The accelerometers placed on the center panels show a peak at a frequency of around 11.5 Hz, which verifies the value of the natural frequency of the first mode of vibration obtained from the RD technique. Interestingly, the accelerometer placed on the foot of the racking system

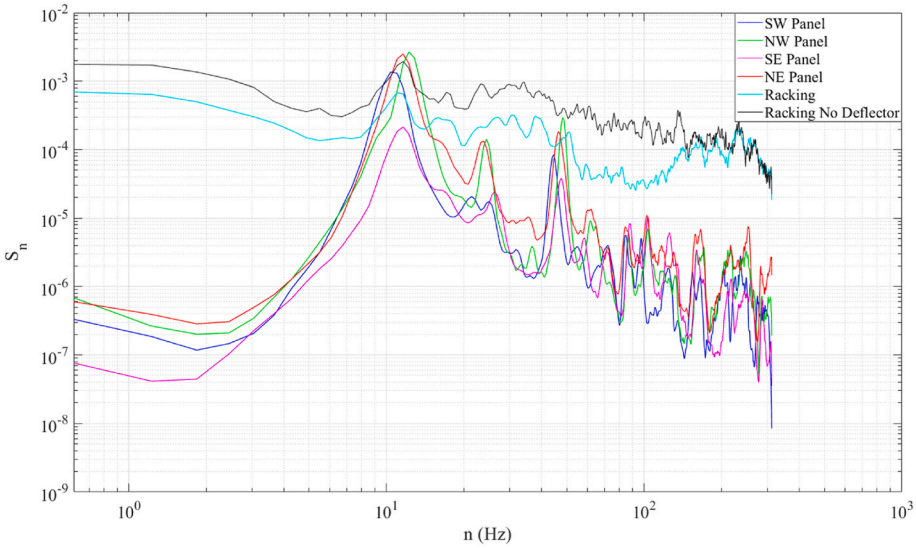

Fig. 17. Accelerations Spectra for a mean wind speed $\overline{U} = 27$ m/s (60 mph).

also shows the largest spike at a frequency $f_n = 11$ *Hz*, which indicates that this is a close enough value for the natural frequency of the system. The reason is that the PV modules' natural frequencies are driving the natural frequency of the system since they are the main source of system vibrations. It is worth noting that this natural frequency may change depending on the size and weight of the modules.

Furthermore, Fig. 17 depicts the acceleration spectrum of the accelerometer on the racking system for the case without wind deflectors. Comparing the spectra of both cases, they both feature a noticeable peak at identical frequency values, suggesting that the addition of deflectors does not alter the dynamic characteristics of the array. Moreover, the case without deflectors displayed a higher spectral density value, indicating an augmentation in the vibrations experienced by the array.

Fig. 18 presents the calculated dynamic amplification factors (DAF) as a function of the reduced mean wind speed at the mean roof height. For comparison with other PV modules featuring different natural frequencies and panel sizes, the wind speed was normalized by the product of the panel's natural frequency (f_n) and panel width (L_c). The expected trend of increasing DAF with rising wind speed is clearly observed, as higher wind speeds lead to stronger vibrations.

It was observed that for the first four reduced wind speeds, corresponding to wind speeds of 30, 40, 50, and 60 mph, increases in wind speed did not affect the DAF values. The DAF remained fairly constant, around 1.2 for an array with wind deflectors and 1.13 for an array without wind deflectors. The DAF for the case where wind deflectors are used increased from 1.20 at a reduced wind speed of 0.8, corresponding to 15.2 m/s (34 mph) to 1.32 at a reduced wind speed of 2.9 corresponding to 52 m/s (117 mph). The addition of wind deflectors increased the dynamic amplification factor by around 10% at higher wind speeds. The reason behind that may be the vibration of the wind deflectors which may change the forcing frequency of wind loads in their wake. Hence, the deflector's design may alter the dynamic loading. Since the DAF is dependent on the system characteristics, it is recommended to assess different ballasted PV systems to evaluate the variation in the DAF. Further research is required to properly address and identify these effects.

These results further emphasize the importance of including dynamic effects in the calculation of wind loading on flexible structures. In this particular case, the dynamic effects increased the area-averaged uplift coefficient on the PV array by 20% at lower wind speeds and by up to 32% as the wind speed reached 52 m/s (117 mph).

3.7. Failure assessment

The findings of this study highlighted that wind loads on ballasted PV systems are dictated by wind direction, shielding, and presence of wind deflectors. Nevertheless, the response of the ballasted system under these wind loads depends not only on the mentioned factors, but also on the weight of the used ballast. The purpose of this section is to compare the effectiveness of different ballast configurations and layouts, as well as the effect of wet conditions which often accompany extreme wind events, on the wind resistance of the ballasted PV system under study. This is achieved by varying the added ballast weights and conducting tests using wind driven rain simulation to evaluate the effect of a damp roof surface during hurricane events on the sliding of the array.

For all the tested cases in the high-speed failure assessment, the critical wind direction was $\theta = 45°$ degrees for all ballast configurations, and for dry and wet conditions. Sliding wind speed, as well as maximum sliding distance were observed for cornering winds $(\theta = 45°)$, followed by normal winds from wind direction $\theta = 0°$, followed by side winds from wind direction $\theta = 90°$. This observation was foreseen, since the results of the aerodynamic testing showed that the wind loading was most critical for cornering wind directions, specifically $\theta = 45°$. For all wind directions, the sliding wind speed was observed to increase with the increase of the number of ballasts added to the array.

Moreover, the results reveal that wet testing conditions do not influence the sliding behavior of the array, even wetting the TPO for a duration before testing had no effect. It was noticed that the sliding wind speeds for the same ballast configurations were identical, regardless of wet or dry testing conditions. For instance, the sliding wind speed for configuration A was 27 m/s (60 mph), for configuration B was 30 m/s (68 mph), and for configuration C was 34 m/s (76 mph) for the critical cornering wind direction $\theta = 45°$, and for wet and dry testing conditions. This outcome can be attributed to the fact that sliding phenomenon does not involve actual sliding motion, but instead, high frequency vibrations where intermittent displacements of the foot resulted in intermittent loss of contact between the corner supports of the system and the roof, which finally led to notable sliding after several cycles. The vibration of the entire system is a result of the wind induced vibrations of the PV panels themselves which are evident in the recorded videos of the test. Further, the high frequency vibrations of the wind deflectors were also observed, which may be an additional factor that worsens the vibration of the entire system. As mentioned earlier, different deflector stiffnesses may have varying DAF, which may affect these results.

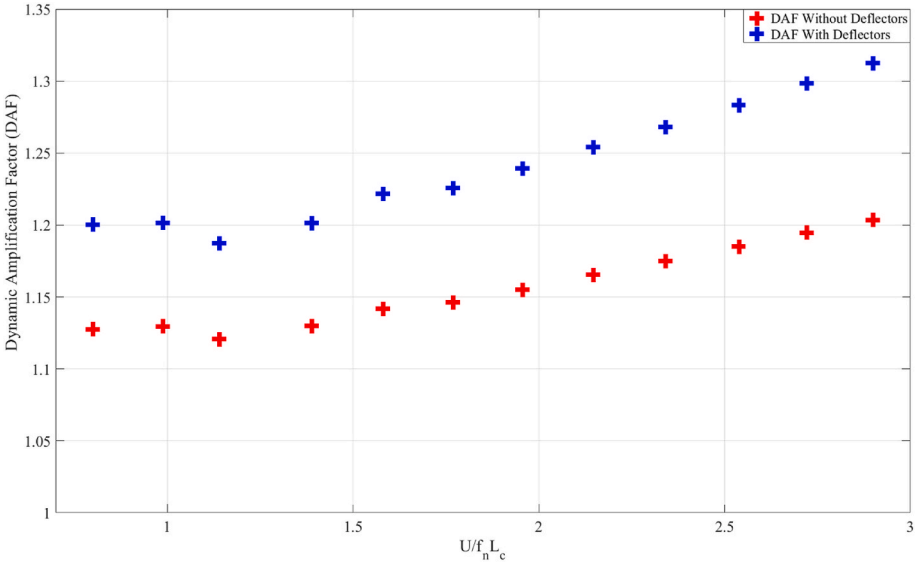

Fig. 18. DAF as a function of reduced wind speed.

Ballasted PV arrays typically consist of multiple rows, each with several modules, to efficiently utilize the entire roof area generating the necessary power for the structure's functionality. As discussed in the aerodynamic loads section, the distribution of wind loading across these systems is not uniform. In the current study, the size of the array was limited by the WOW flow field, resulting in a setup that resembles a corner section of a larger array. The corner modules are likely to experience the most intense wind loading as conical vortices form at the structure's corners, followed by the edge modules that face high suctions due to flow separation at the roof's edge. In contrast, the internal modules of the arrays encounter reduced wind loading due to the shielding effects from external modules as well as their positioning away from the edges and corners. It must be noted that the aerodynamic loads may change with changing the test setup, a different geometry may lead to a shift in the location and magnitude of the maximum aerodynamic loads. The sliding of the system at the reported wind speeds in this study is unlikely to occur in such large arrays. This is explained by the large number of modules and ballast which increase the overall weight of the system, as well as the higher number of contact points with the roof which lead to an increased frictional resisting force. These enhancements in the systems' resistance are not met with a proportional increase of wind loading, (decreased wind loading on internal modules that form most of the array), consequently reducing the likelihood of a sliding failure mode. Therefore, restricted from sliding, the most probable failure in these systems is the uplift failure of the corner or edge modules.

To achieve the desired uplift failure without risking the sliding of the entire system off the roof, the four front supports of the array were mechanically fastened to the roof while leaving the other eight unaltered. This simulates the sliding restriction in a typical PV array. During the test, the vibrations of the system were similar to the previous tests performed, however with the increase in wind speed, considerable lifts of the windward supports were noticed until one lift was significant enough for the wind to get underneath the system and flip it off the entire roof. This is an interesting observation, because as discussed previously, high wind loads on smaller areas of the panel, in addition to the unpredictable vibrations of the ballasted system may initiate lifts in one or more of the supports and result in a cascading type of failure. It was also observed that the modules disengaged from the racking system before flying away and started acting as windborne debris. This uplift phenomenon may cause damage to the surrounding modules and/or the surrounding built environment.

To evaluate the efficacy of the analytically compensated pressure coefficients for dynamic effects, the failure wind speed was first estimated using the obtained pressure coefficients from the aerodynamic (rigid model) test. Then it was reevaluated using the pressure coefficients compensated for dynamic effects.

The pressure coefficients were obtained by area averaging the time histories over the NE panel (the first panel lifted by wind) before generating the peaks by applying the specific static or dynamic compensation method. Following this, equation (4) can be reformulated to derive the expression for the wind uplift force [see equation (11)]. It must be noted that the term $\cos(10^\circ)$ was included in equation (11) since the uplift force acts normal to the surface of the panel, which is inclined at a 10° angle.

$$F = \widehat{C_p} \times 0.5 \times \rho \times U^2 \times A \times \cos(10^\circ) \tag{11}$$

By equating the above estimated wind uplift force to the total weight of the NE panel (including the weight of the racking system and ballasts), and solving for U in the above equation, the failure wind speed was obtained.

Finally, a comparison was made between the estimated and the actual failure wind speed witnessed in the WOW EF. Table 2 provides a summary of the estimated failure wind speeds derived from both the statically and dynamically compensated pressure coefficients and compares them to the observed failure wind speed. The estimated failure wind speed using the dynamically compensated pressure coefficient closely matched the observed failure wind speed, in contrast to the failure wind speed estimated from the peak pressure coefficients not compensated for dynamic effects, which was 115 mph, exceeding the observed failure wind speed by 12 mph. This asserts the requirement of including wind induced dynamic effects in the design of ballasted PV arrays.

Table 2
Comparison of estimated and observed failure wind speeds.

	Peak Pressure Coefficient ($\widehat{C_p}$)	Estimated failure wind speed (mph)	Observed failure wind speed (mph)
Peak compensation (no dynamic effects)	0.51	115.5	103
Peak compensation (with dynamic effects)	0.663	101	

4. Conclusion

This research work is an effort to acquire deeper insights into the performance of ballasted PV arrays exposed to extreme wind events, as well as the mitigation aspect of wind deflectors typically added to those arrays. The study considered a 2 x 2 ballasted PV array resembling an array close to the corner of a flat roofed building. This corner was subjected to full-scale aerodynamic, dynamic, and destructive experiments in the NSF-supported NHERI WOW EF at FIU. Comparisons of mean and peak point pressure coefficients as well as area-averaged coefficients for each panel and for the entire array were performed for the array for two configurations: (1) with wind deflectors and (2) without wind deflectors. Moreover, the power spectral densities of individual taps and the correlation between them were evaluated. The key findings of this study are summarized below.

- Wind deflectors were efficient in dissipating the effects of conical vortices on windward panels, reducing mean and peak pressure coefficient values for individual pressure taps for cornering wind directions by up to 50%. However, for normal winds ($\theta = 0^\circ$) and cornering winds ($\theta = 90^\circ$), the mitigation effect was not evident.
- The area-averaged pressure coefficients on the top surface of the panels were shown to be unaltered by the addition of wind deflectors. In contrast, wind deflectors reduced the area-averaged pressure coefficients on the bottom surface of the panels. This reduction results in a reduced pressure on the underside of the panels which attempts to push the panel away from the roof, consequently reducing the net uplift on the panels. The reduction as most pronounced for cornering wind directions ($\theta = 30^\circ - 60^\circ$) for the NE and SE panels. NW and SW panels experienced reduced wind loading due to shielding effects from the NE and SE windward panels.
- Power spectral density (PSD) values, and consequently RMS values of pressure fluctuations in regions dominated by conical vortices, showed the greatest reduction following the addition of wind deflectors. This reduction was less pronounced for edge taps unaffected by conical vortices and for internal taps.
- The worst area-averaged peak force coefficients from all wind directions and for all combinations of pressure taps' tributary areas showed that ASCE 7–22 envelope for rooftop solar panels can be considered conservative. However, a considerable number of outlying points were observed to exceed the envelope for smaller areas. This requires careful consideration especially for the case of ballasted PV panels which have no physical connection to the roof.
- The addition of wind deflectors was shown to disrupt the correlation between instantaneous aerodynamic pressures occurring at different

locations on the array. Hence, the reduction of net uplift is primarily due to preventing peak pressures from occurring simultaneously, rather than from reductions in the peak values of individual taps, where only individual pressure coefficients in the vicinity of conical vortices were reduced.

- The wind-induced vibrations of the array could increase the loading by up to 30% at higher wind speeds. This further emphasizes the necessity to consider wind induced dynamic effects in the design of ballasted PV arrays.
- Wet conditions, commonly associated with wind-driven rain during hurricane events, have minimal effects on the sliding of the array (however, more studies are needed to ascertain this finding).
- The uplift failure mode is initiated by loss of contacts for one or more of the supports, followed by a cascading effect where the subsequent panels are lifted due to the interconnectedness. This causes an abrupt change in the aerodynamics and ultimately leads to the system lifting off the roof.

It must be mentioned that this study only covered a single style of mounting systems with rear wind deflectors, so the results and conclusions are only applicable to this specific scenario.

Expanding this experimental endeavor can involve further research to explore the effect of varying edge distances, the incorporation of side deflectors, and the use of panels with larger sizes, which are becoming more common nowadays, on wind loading and the mitigation effect of wind deflectors. Furthermore, future studies are encouraged to conduct a parametric study on the effect of deflectors with different stiffnesses or geometric shapes to produce the optimal characteristics for the most efficient type of wind deflectors.

CRediT authorship contribution statement

Houssam Al Sayegh: Writing – review & editing, Writing – original draft, Methodology, Formal analysis, Conceptualization. **Arindam Gan Chowdhury:** Writing – review & editing, Supervision, Resources, Funding acquisition, Conceptualization. **Ioannis Zisis:** Writing – review & editing, Supervision, Resources, Funding acquisition, Conceptualization. **Amal Elawady:** Writing – review & editing, Methodology. **Johnny Estephan:** Writing – review & editing, Methodology. **Ameyu Tolera:** Writing – review & editing, Methodology.

Declaration of competing interest

The authors declare that they have no known competing financial interests or personal relationships that could have appeared to influence the work reported in this paper.

Acknowledgement

The study was funded by the National Science Foundation (NSF) through the Industry/University Cooperative Research Center (IUCRC) to the Wind Hazard Infrastructure Performance (WHIP) Center at Florida International University (FIU) (award numbers 1520853, 1841503, and 2037899). The experiments were greatly facilitated by the help of WOW staff members James Erwin, Dr. Manuel Matus, Dr. Steven Diaz, Dr. Dejiang Chen and Walter Conklin. The opinions, findings, conclusions, or recommendations expressed in this article are solely those of the authors and do not represent the opinions of the funding agencies.

Data availability

The authors do not have permission to share data.

References

Abiola-Ogedengbe, A., Hangan, H., Siddiqui, K., 2015. Experimental investigation of wind effects on a standalone photovoltaic (PV) module. Renew. Energy 78, 657–665. https://doi.org/10.1016/j.renene.2015.01.037.

Acosta, T.J., Guo, Y., Wang, J., Brusco, S., Kopp, G.A., 2024. Requirements for partial turbulence simulations using nondimensional turbulence energy contributions. J. Wind Eng. Ind. Aerod. 254, 105886.

Alawode, K.J., Vutukuru, K.S., Elawady, A., Lee, S.J., Chowdhury, A.G., Lori, G., 2023. Wind-induced vibration and wind-driven rain performance of a full-scale single-skin facade unit with vertical protrusions. J. Architect. Eng. 29 (2). https://doi.org/10.1061/jaeied.aeeng-1393.

Aly, A.M., Clarke, J., 2023. Wind design of solar panels for resilient and green communities: CFD with machine learning. Sustain. Cities Soc. 94. https://doi.org/10.1016/j.scs.2023.104529.

American Society of Civil Engineers, Minimum Design Loads and Associated Criteria for Buildings and Other Structures.

Asghari Mooneghi, M., Irwin, P., Gan Chowdhury, A., 2016. Partial turbulence simulation method for predicting peak wind loads on small structures and building appurtenances. J. Wind Eng. Ind. Aerod. 157, 47–62. https://doi.org/10.1016/j.jweia.2016.08.003.

Azzi, Z., Habte, F., Vutukuru, K.S., Gan Chowdhury, A., Moravej, M., 2020a. Effects of roof geometric details on aerodynamic performance of standing seam metal roofs. Eng. Struct. 225 (Dec). https://doi.org/10.1016/j.engstruct.2020.111303.

Azzi, Z., Habte, F., Elawady, A., Gan Chowdhury, A., Moravej, M., 2020b. Aerodynamic mitigation of wind uplift on low-rise building roof using large-scale testing. Front Built Environ 5 (Jan). https://doi.org/10.3389/fbuil.2019.00149.

Banks, D., 2013. The role of corner vortices in dictating peak wind loads on tilted flat solar panels mounted on large, flat roofs. J. Wind Eng. Ind. Aerod. 123, 192–201. https://doi.org/10.1016/j.jweia.2013.08.015.

Banks, D., Guha, T.K., Fewless, Y.J., 2015. A hybrid method of generating realistic full-scale time series of wind loads from large-scale wind tunnel studies: application to solar arrays. In: 14th International Conference on Wind Engineering, pp. 21–26.

Browne, M.T.L., Gibbons, M.P.M., Gamble, S., Galsworthy, J., 2013. Wind loading on tilted roof-top solar arrays: the parapet effect. J. Wind Eng. Ind. Aerod. 123, 202–213. https://doi.org/10.1016/j.jweia.2013.08.013.

Burgess, C., Goodman, J., 2018. Solar under storm. Select best practices for resilient ground-mount PV systems with hurricane exposure. https://rmi.org/wpcontent/uploads/2018/06/Islands_SolarUnderStorm_Report_digitalJune122018.pdf. (Accessed 1 January 2023).

Choi, S.M., Lee, G.R., Park, C.D., Cho, S.H., Lim, B.J., 2021. Wind load on the solar panel array of a floating photovoltaic system under extreme hurricane conditions. Sustain. Energy Technol. Assessments 48. https://doi.org/10.1016/j.seta.2021.101616.

Cochran, L.S., English, E.C., 1997. Reduction of roof wind loads by architectural features. Archit Sci Rev 40 (3), 79–87. https://doi.org/10.1080/00038628.1997.9697388.

Enshaei, P., Chowdhury, J., Sauder, H., Banks, D., 2023. Wind tunnel testing of torsional instability in single-Axis solar trackers: summary of methodologies and results. In: AWESW2022: 21th Australasian Wind Engineering Society Workshop.

ESDU (Engineering Sciences Data Unit), 2001. Characteristics of the at-mospheric boundary layer, Part II: single point data for strongwinds (neutral atmosphere). ESDU Item 85020. ESDU, London.

Estephan, Johnny, 2022. Hybrid Experimental-Numerical Methodology and Field Calibration for Prediction of Peak Wind Effects on Low-Rise Buildings and Their Appurtenances, vol. 5154. FIU Electronic Theses and Dissertations. https://digitalcommons.fiu.edu/etd/5154.

Estephan, J., Gan Chowdhury, A., Elawady, A., Erwin, J., 2021. Dependence of internal pressure in low-rise buildings on aerodynamic parameters, defect features and background leakage. J. Wind Eng. Ind. Aerod. 219 (Dec). https://doi.org/10.1016/j.jweia.2021.104822.

Estephan, J., Gan Chowdhury, A., Irwin, P., 2022. A new experimental-numerical approach to estimate peak wind loads on roof-mounted photovoltaic systems by incorporating inflow turbulence and dynamic effects. Eng. Struct. 252 (Feb). https://doi.org/10.1016/j.engstruct.2021.113739.

Feldman, D., Margolis, R., Goodrich, A., Barbose, G., Wiser, R., Darghouth, N., 2012. Photovoltaic (PV) pricing trends: historical, recent, and near-term projections [Online]. Available: www.lbl.gov.

Gan Chowdhury, A., et al., 2017. Large-scale experimentation using the 12-fan Wall of wind to assess and mitigate hurricane wind and rain impacts on buildings and infrastructure systems. J. Struct. Eng. 143 (7). https://doi.org/10.1061/(asce)st.1943-541x.0001785.

Geurts, C.P., van Bentum, C.A., 2014. A novel guideline for wind loads on solar energy systems. ICBEST 2014, 9–12.

Guo, Y., Wu, C.H., Kopp, G.A., 2021. A method to estimate peak pressures on low-rise building models based on quasi-steady theory and partial turbulence analysis. J. Wind Eng. Ind. Aerod. 218, 104785 t.

Holmes, J.D., 2015. Wind Loading of Structures, third ed. CRC Press. https://doi.org/10.1201/b18029.

Irwin, P.A., 2009. Wind engineering research needs, building codes and project specific studies. In: 11th Am Conf Wind Eng.

Irwin, H.P.A.H., Cooper, K.R., Girard, R., 1979. Correction of distortion effects caused by tubing systems in measurements of fluctuating pressures. J. Wind Eng. Ind. Aerod. 5 (1–2), 93–107.

Jeary, A.P., 1992. Establishing non-linear damping characteristics of structures from non-stationary response time-histories. Struct. Eng. 70 (4), 61–66.

Katsuchi, H., Yamada, H., 2011. Study on turbulence partial simulation for wind-tunnel testing of bridge deck. In: Proc. Of ICWE, vol. 13.

Kern, Edward C. Ballast-mounted PV arrays: Phase 2 final report. United States. https://doi.org/10.2172/764761.
Kopp, G.A., 2014. Wind loads on low-profile, tilted, solar arrays placed on large, flat, low-rise building roofs. J. Struct. Eng. 140 (2), 04013057.
Kopp, G.A., 2023. Updates to the wind tunnel method for determining design loads in ASCE 49-21. Wind Struct. 37 (2), 163–178.
Kopp, G.A., Banks, D., 2012. Use of the wind tunnel test method for obtaining design wind loads on roof-mounted solar arrays. J. Struct. Eng. 139, 284–287.
Kopp, G.A., Farquhar, S., Morrison, M.J., 2012. Aerodynamic mechanisms for wind loads on tilted, roof-mounted, solar arrays. J. Wind Eng. Ind. Aerod. 111, 40–52. https://doi.org/10.1016/j.jweia.2012.08.004.
Kudav, G.V., Panta, Y.M., Yatsco, M., 2012. Design and testing of wind deflectors for roof-mounted solar panels. In: WIT Transactions on Engineering Sciences, pp. 15–27. https://doi.org/10.2495/AFM120021.
Matus, M.A., 2018. Experimental Investigation of Wind-Induced Response of Span-Wire Traffic Signal Systems.
Melbourne, W.H., 1979. Turbulence effects on maximum surface pressures-a mechanism and possibility of reduction. In: Proc Fifth Int Conf Wind Eng, Fort Collins USA, pp. 541–551.
Mignone, A., Inghirami, G., Rubini, F., Cazzaniga, R., Cicu, M., Rosa-Clot, M., 2021. Numerical simulations of wind-loaded floating solar panels. Sol. Energy 219, 42–49. https://doi.org/10.1016/j.solener.2020.11.079.
Moravej, M., 2018. Investigating Scale Effects on Analytical Methods of Predicting Peak Wind Loads on Buildings. Florida International University. https://doi.org/10.25148/etd.FIDC006834.
Moravej, M., Chowdhury, A.G., Irwin, P., Zisis, I., Bitsuamlak, G., 2015. Dynamic effects of wind loading on photovoltaic systems. In: 14th. International Conference on Wind Engineering (ICWE14). Porto Alegre, Brazil.
Moravej, M., Estephan, J., Irwin, P., Chowdhury, A.G., 2024. Scaling effects on peak wind load estimation for low-rise buildings: an experimental and analytical study. Eng. Struct. 316, 118499.
Morrison, M.J., Kopp, G.A., 2018. Effects of turbulence intensity and scale on surface pressure fluctuations on the roof of a low-rise building in the atmospheric boundary layer. J. Wind Eng. Ind. Aerod. 183, 140–151.
Naeiji, A., Raji, F., Zisis, I., 1868. Large-scale wind testing of photovoltaic panels mounted on residential roofs. In: Structures Congress 2015, pp. 1868–1878.
Naeiji, A., Raji, F., Zisis, I., 2017. Wind loads on residential scale rooftop photovoltaic panels. J. Wind Eng. Ind. Aerod. 168, 228–246. https://doi.org/10.1016/j.jweia.2017.06.006.
Richards, P.J., Hoxey, R.P., Connell, B.D., Lander, D.P., 2007. Wind-tunnel modelling of the silsoe cube. J. Wind Eng. Ind. Aerod. 95 (9–11), 1384–1399.
Richards, P., Asghari Mooneghi, M., Chowdhury, A.G., 2015. Combining directionality narrow band wind loading data to match wide band full-scale simulations. In: 14th International Conference on Wind Engineering. Porto Alegre, Brazil.
Sangchuwong, P., Yamada, H., Katsuchi, H., 2013. Study on Turbulence Effects on Flow Fields Around Sharp-Edged Bluff Bodies 2013, p. 59A.
Schellenberg, A., Maffei, J., Telleen, K., Ward, R., 2013. Structural analysis and application of wind loads to solar arrays. J. Wind Eng. Ind. Aerod. 123, 261–272. https://doi.org/10.1016/j.jweia.2013.06.011.
Stathopoulos, T., Baskaran, A., 1987. Wind pressures on flat roofs with parapets. J. Struct. Eng. 113 (11), 2166–2180.
Stathopoulos, T., Zisis, I., Xypnitou, E., 2012. Wind loads on solar collectors: a review. In: Structures Congress 2012, pp. 1169–1179.
Stathopoulos, T., Zisis, I., Xypnitou, E., 2014. Local and overall wind pressure and force coefficients for solar panels. J. Wind Eng. Ind. Aerod. 125, 195–206. https://doi.org/10.1016/j.jweia.2013.12.007.
Stone, L., Burgess, C., Locke, J., 2020. Solar under the storm for policymakers: select best practices for resilient photovoltaic systems for small island developing states. www.rmi.org/insight/solar-under-storm/. (Accessed 1 January 2023).
Suaris, W., Irwin, P., 2010. Effect of roof-edge parapets on mitigating extreme roof suctions. J. Wind Eng. Ind. Aerod. 98 (10–11), 483–491. https://doi.org/10.1016/j.jweia.2010.03.001.
Surry, D., Lin, J.X., 1995. The effect of surroundings and roof corner geometric modifications on roof pressures on low-rise buildings. J. Wind Eng. Ind. Aerod. 58 (1–2), 113–138.
Tamura, Y., Suganuma, S.Y., 1996. Evaluation of amplitude-dependent damping and natural frequency of buildings during strong winds. J. Wind Eng. Ind. Aerod. 59 (2–3), 115–130.
Tieleman, H.W., 2003. Wind tunnel simulation of wind loading on low-rise structures: a review. J. Wind Eng. Ind. Aerod. 91, 1627–1649.
Tokay, A., Petersen, W.A., Gatlin, P., Wingo, M., 2013. Comparison of raindrop size distribution measurements by collocated disdrometers. J. Atmos. Ocean. Technol. 30 (8), 1672–1690. https://doi.org/10.1175/JTECH-D-12-00163.1.
Tolera, A.B., Mostafa, K., Chowdhury, A.G., Zisis, I., Irwin, P., 2022. Study of wind loads on asphalt shingles using full-scale experimentation. J. Wind Eng. Ind. Aerod. 225 (Jun). https://doi.org/10.1016/j.jweia.2022.105005.
Vutukuru, K.S., Moravej, M., Elawady, A., Chowdhury, A.G., 2020. Holistic testing to determine quantitative wind-driven rain intrusion for shuttered and impact resistant windows. J. Wind Eng. Ind. Aerod. 206. https://doi.org/10.1016/j.jweia.2020.104359.
Yamada, H., Katsuchi, H., 2008. Wind-tunnel study on effects of small-scale turbulence on flow patterns around rectangular cylinder. In: 6th Int. Colloquium on Bluff Bodies Aerodynamics & Applications, International Association of Wind Engineering. Kanagawa, Japan.
U.S. Solar Market Insight." Accessed: May 23, 2023. [Online]. Available: https://www.seia.org/.
Wind tunnel testing for buildings and other structures. ASCE Standard 49–12, 2012, 1–54. https://doi.org/10.1061/9780784415740.